TECHNICAL MEMORANDUM **MAE-TM-25**

Analysis of Opposed Jet Hydrogen-Air Counter Flow Diffusion Flame

Y. H. Ho
and
K. M. Isaac

Prepared Under NASA Langley Research Center Grant NAG-1-861

October 1989

MECHANICAL AND AEROSPACE ENGINEERING
AND ENGINEERING MECHANICS DEPARTMENT
UNIVERSITY OF MISSOURI-ROLLA

ABSTRACT

A computational simulation of the opposed-jet diffusion flame is performed to study its structure and extinction limits. The present analysis concentrates on the nitrogen-diluted hydrogen-air diffusion flame, which provides the basic information for many vehicle designs such as the aerospace plane for which hydrogen is a candidate as the fuel. The computer program uses the time-marching technique to solve the energy and species equations coupled with the momentum equation solved by the collocation method. The procedure is implemented in two stages. In the first stage, a one-step forward overal chemical reaction is chosen with the gas phase chemical reaction rate determined by comparison with experimental data. In the second stage, a complete chemical reaction mechanism is introduced with detailed thermodynamic and transport property calculations. Comparison between experimental extinction data and theoretical predictions is discussed. The effects of thermal diffusion as well as Lewis number and Prandtl number variations on the diffusion flame are also presented.

ACKNOWLEDGEMENT

The Hypersonic Propulsion Branch at the NASA Langley Research Center has provided financial support for this project under NASA Grant NAG-1-861. Dr. Gerald L. Pellett is the technical monitor. Their sponsorship is gratefully acknowledged. The authors would like to thank the following persons for their help during this effort: Dr. H. S. Mukunda for the fruitful discussions regarding the nature of diffusion flames and the formulation of the problem and Dr. Robert Kee for providing the CHEMKIN routines. Dr. G. B. Northam, Dr. C. Jachimowski, Dr. T. Chitsomboom, Dr. R. C. Rogers, Dr. P. Drummond and several others at the Langley Research Center showed interest and moral support towards this project. Above all, Dr. Pellett showed great optimism and confidence in us when we were struggling with initial profiles and other such matters concerning the numerical solution of the equations. His patience and encouragement are gratefully acknowledged.

TABLE OF CONTENTS

LIST OF ILLUSTRATIONS

LIST OF TABLES

NOMENCLATURE

A	Coefficient in Equation (61)
A_m	The pre-exponential factor
A^*_{ik}	Coefficient in Equation (B.39)
a	Strain rate (du_e/dx)
a_{ki}	Coefficient in Equation (37) ($k = 1, ...,7$)
B	Body force
B_i	Coefficients in Equation (62)
B^*_{ik}	Coefficient in Equation (B.40)
b_{ki}	Coefficient in Equation (B.4) ($k = 1,...,4$)
C^*_{ik}	Coefficient in Equation (B.41)
C	$\rho\mu/\rho_e\mu_e$
$\dot{C}_i'''$	Creation rate
c_i	Mass fraction of species i
c_p	Constant pressure specific heat
$\overline{c_p}$	Defined by Equation (13)
c_v	Constant volume specific heat
D	Diffusion Coefficient
$\dot{D}_i'''$	Destruction rate
D^T	Thermal diffusion Coefficient
D_I	Damköhler number
d	Diameter of the jet
E_j	Coefficients in Equation (61)
E_H	Hydrogen activation energy
E_m	The activation energy in Equation (52)
e_i	Internal energy of species i

F_{trans}, F_{rot}, F_{vib}	Coefficients in Equation (B.4)
f	Similarity parameter
g	Normalized enthalpy (Equation 26)
H	Width of the jet
h	Mixture enthalpy
h_i	Enthalpy of species i
h_i°	Formation enthalpy of species i
k_{cm}	The equilibrium constant
k_{fm}	The forward rate constant
k_{rm}	The reverse rate constant
L_{ei}	Lewis number
L_{ei}^T	Thermal Lewis number
M	Molecular weight
n	index for two dimensional flow (n = 0) or axisymmetric flow (n = 1)
nr	Number of reactions
ns	Number of species
P_r	Prandtl number
P	Coefficient in Equation (B.34)
P_{atm}	Atmospheric pressure,
p	Pressure
Q	Coefficient in Equation (B.34)
q_m	Rate of progress variable
$\vec{q}$	Velocity vector
$\vec{q}_i$	Diffusional velocity vector of species i
R_i	Gas constant of species i
R_U	Universal gas constant

S_j	Coefficients in Equation (62)
T	Temperature
t	Time
U_{rot}	Rotational relaxation collision number
u	Velocity in x direction
V_{i_v}	Thermal diffusion velocity
v	Normal velocity
W	Molecule mass
$\dot{w}'''$	Production rate
X	Mole fraction
[X]	Mole concentration
x	x coordinate (normal to stagnation plane)
Y	Normalized mass fraction (Equation 27)
x_v	Spatial coordinate in Equation (B.42)
y	y coordinate (tangent to stagnation plane)
Z_H	Hydrogen reaction rate constant
α	Polarizability
$\overline{\alpha}$	The efficiency factor in Equation (54)
β_m	The temperature exponent
X	Coefficient in Equation (B.33)
χ_i	the chemical symbol for species i
Δ	Grid spacing increment
δ^*	Coefficient in Equation (B.2)
ε	Lennard-Jones potential well depth
η	Coordinate of the similarity transformation (17)
Γ	Coefficient in Equation (B.8)
γ	Index in Equation (45)

Λ	Coefficient in Equation (B.19)
K_B	The Boltzmann constant
κ	Thermal conductivity
μ	Viscosity
Ω	Collision integral
Φ	Dissipation function
ϕ	Coefficient in Equation (B.43)
Ψ	Viscous terms that are addition to those expressed by $div\,(\mu\ grad\,\vec{q})$
ψ	Stream function
ρ	Density
σ	Lennard-Jones collision diameter
Θ	Thermal diffusion ratio
θ	Normalized temperature (Equation 28)
τ	Dipole moment
Υ	Coefficient in Equation (B.9)
$\upsilon_{i\,m}$	Stoichiometric coefficients
ξ	Coordinate of the similarity transformation (18)
ζ	Coefficient in Equation (B.28)

Subscripts

i	ith component of mixture
j	jth node of computation domain
e	Boundary layer edge condition; right hand side control surface
w	left hand side control surface

I. INTRODUCTION

The study of stationary flames, as opposed to propagating or explosive flames, may be generally divided into two classes, the premixed flame and the diffusion flame. In the premixed flame, the fuel and air or oxygen are premixed before entering the reaction zone. Normally, the gases of premixed flames start with a high chemical potential, which breaks down suddenly in the reaction zone. When the composition (the kinds of fuel and oxidizer and their mixture ratio) and the physical conditions (the pressure and the temperature) are specified, the final combustion state and the characteristics of the flame can be determined uniquely. If mixing occurs rapidly compared with combustion reactions or well ahead of the flame zone, burning can be considered in terms of homogeneous process, or premixed flame. However, there are systems in which mixing controls the burning rate. Most practical systems fall in this category, and they are the so-called diffusion flames.

In the diffusion flame, the fuel and oxidant are initially separated and the reactants mix in the same region in which reactions take place. For the diffusion flame, unlike the premixed flame, we have no high chemical potential (there may be a small potential on the fuel side due to a delay in its breakdown into its elements). Therefore, diffusion flames differ from premixed flames in that the combustion occurs at the interface between the fuel and the oxidizer, and the burning processes are more dependent on the rate of inter-diffusion of the fuel and oxidant than on the rates of the chemical reactions involved. For this reason, the aerodynamic nature of the flow is an important factor in the behavior of the diffusion flame. The main difficulty with diffusion flames is that they do not propagate and, therefore, there are no fundamental characteristics like flame velocity which can be readily measured in premixed flames. This is also part of the reason that diffusion flames have received less attention than

premixed flames in earlier years, despite the fact that diffusion flames have greater practical applications and are encountered more frequently.

The problem of ignition and extinction of flames is of considerable importance to re-entry vehicles; the development of flame due to boundary layer heating of these vehicles is undesirable and in some cases dangerous. If one could predict the extinction speeds for flames in such systems, it would, perhaps, be possible to keep the missile in a velocity spectrum beyond the extinction speeds and thus prevent the onset of flames. Studies of extinction of laminar counterflow diffusion flames will provide a simple model for an accurate understanding of various combustion characteristics closely related to the flame's extinction phenomena as well as a detailed understanding of the structure of the flame. Laminar counterflow diffusion flames can be classified into two large groups : (1) Diffusion flames formed by fuel and oxidant coming from two opposed jets (as shown in Fig. 1). and (2) Diffusion flame in the forward stagnation region of a porous burner, in which a fuel gas is blown from the porous burner into an oncoming oxidizer flow (as illustrated in Fig. 2).

In the present analysis, only the opposed-jet counterflow diffusion flame configuration is selected to analyze the nitrogen-diluted hydrogen-air diffusion flame. However, it is easy to apply the present method to the porous burner case with a few simple modifications. The boundary layer similarity solution is employed with the use of time-marching finite difference technique and one a step second order reaction model. The strain induced extinction at high velocity gradient is investigated and compared with experimental data. The effects of transport property variations on the flame are also examined.

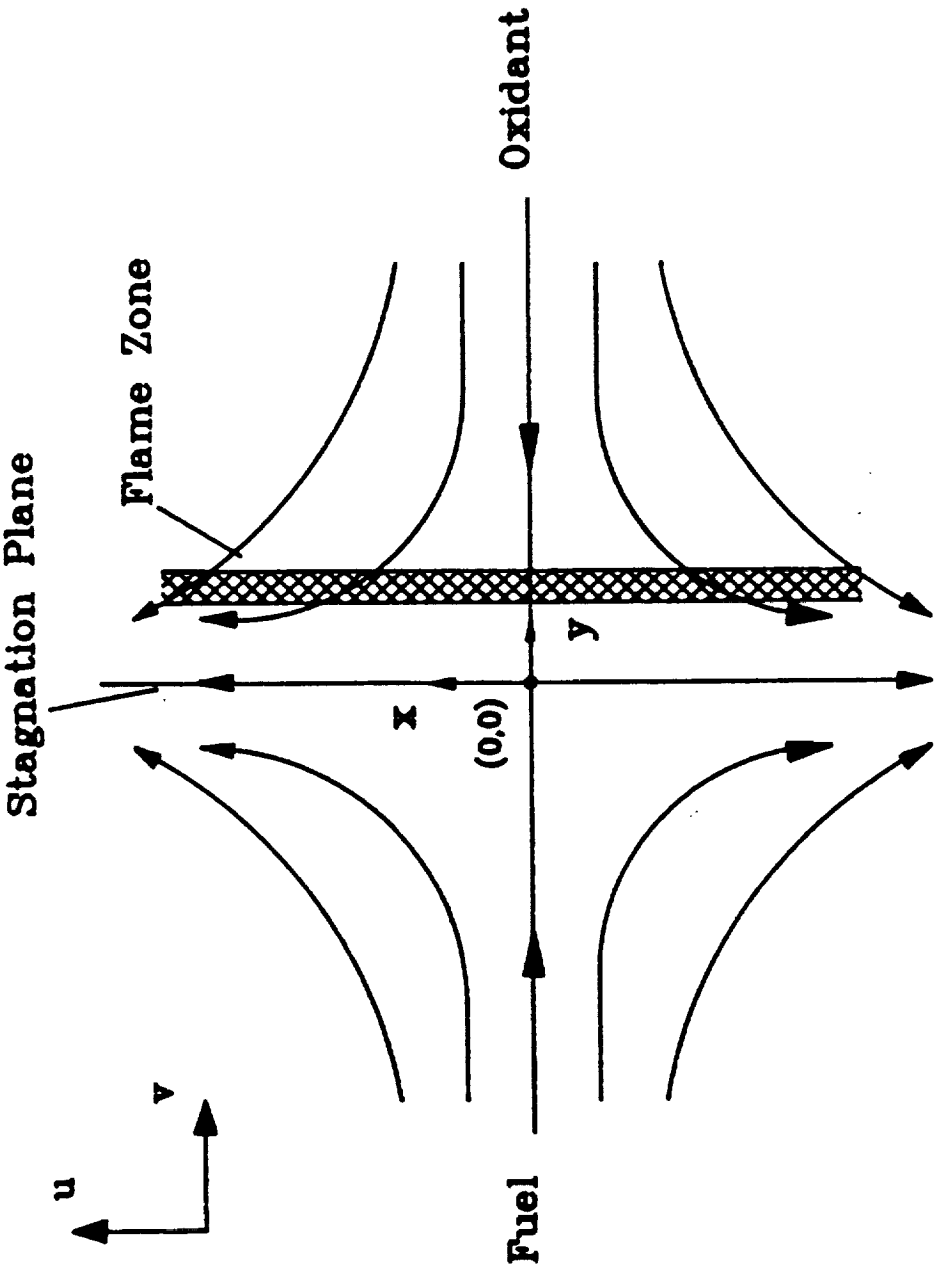

Figure 1. Schematic Diagram of the Opposed-Jet Diffusion Flame.

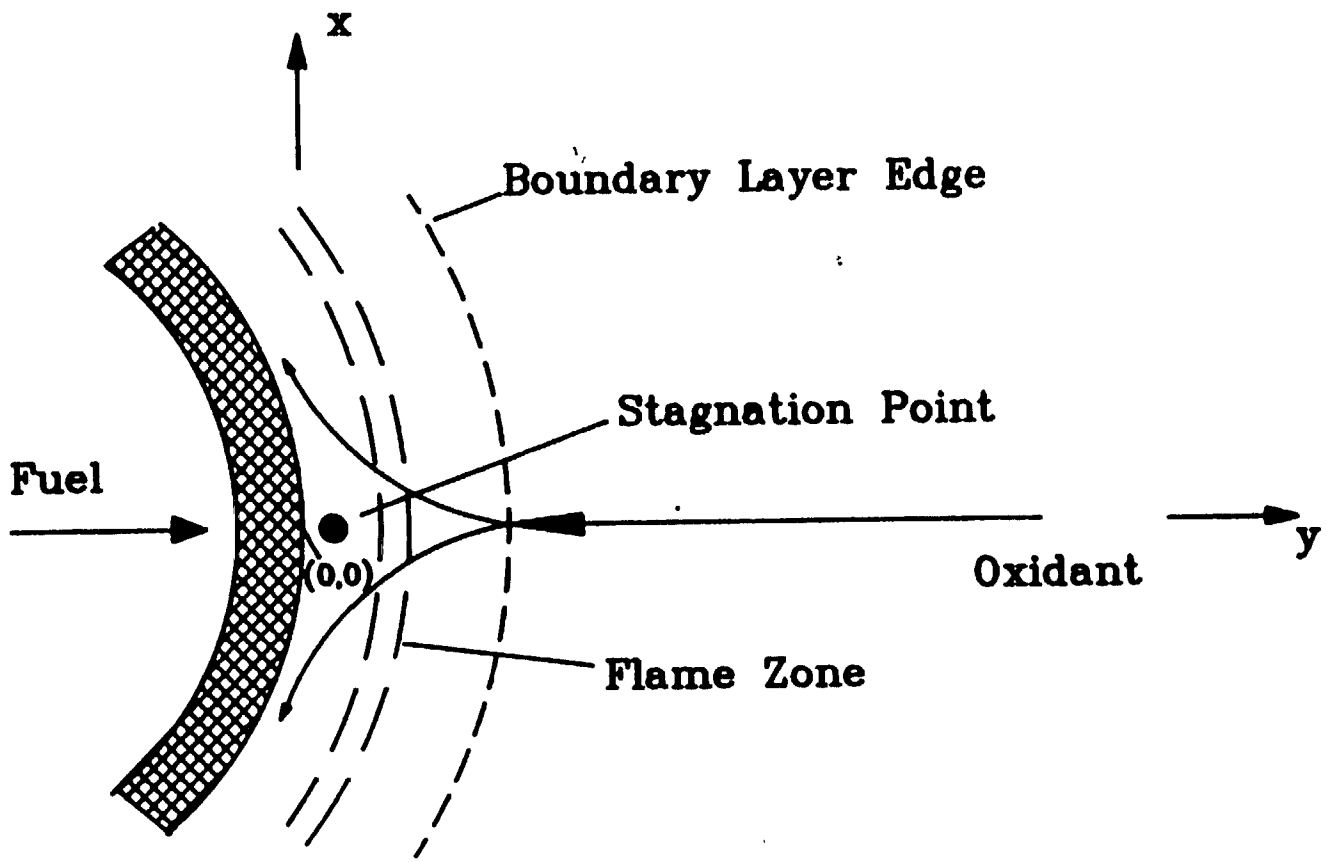

Figure 2. Flow Configuration for the Porous Burner.

II. LITERATURE SURVEY

The main purpose of the present theoretical analysis of the diffusion flame is to examine how the flame zone thickness and the flame temperature vary with the strain induced velocity gradient and/or the reaction rates to determine the critical values of the parameters for flame extinction ; it is also the purpose of the present study to understand clearly the structure of the diffusion flame. Studies on opposed-jet diffusion will help in the evaluation of the chemical kinetic data for fuel-air mixture, especially those which are difficult to handle in the premixed flame.

Some of the pioneering experimental studies on opposed-jet diffusion flame were employed by Potter and Butler [1] and Potter, Heimel, and Butler [2] to obtain information on overall burning rates of a wide variety of fuels. Spalding [3] made analytical studies and obtained an approximate expression for the mass rates at extinction. In his model, he assumed infinitely fast reactions to find the location of the flame front, the rate at which these reactants are consumed, and the volumetric heat release rates. According his theory, the pressure and jet diameter will affect the extinction limits of the flame and he recommend that higher Reynolds number should be used in the experiment to ensure the diffusion flame is well inside a region one-tenth the jet diameter in size, so that the flow can be predicted using his theory. The use of variable properties and more complex chemical kinetic models were suggested. Some of the conclusions of his theory were later verified by the experimental work of Anagnostu and Potter [4].

Fendell [5] considered a model for the extinction of the opposed jet diffusion flame. He used a direct one-step chemical kinetics of finite rate and very high activation energy. The last assumption made it possible to employ asymptotic expansions in his analysis. Chung, Fendell and Holt [6] used a one-step reversible model and found the conditions which distinguish the simple and multiple transition between frozen and

equilibrium state for a given fuel-oxidant system. By employing the asymptotic method, they obtained the various ignition and extinction limits governed by the combination of Damköhler number and equilibrium constant.

Jain and Mukunda [7] considered a compressible flow with Prandtl and Schmidt number taken as unity. By introducing a conserved property parameter, they reduced the range of integration to simplify the numerical analysis. Results for the effects of jet temperature, activation energy and oxidant concentration on the extinction condition were obtained. Jain and Mukunda [8] later considered a system of hydrogen-carbon monoxide fuel mixture. Two one-step reaction schemes were considered and the study revealed that a simple mixing rule can be employed to obtain the mass flow rates at extinction. The computed maximum volumetric heat release rates were compared with experimental data.

In their work on the prediction of flame location in the stagnation point flow with hydrogen injected form porous wall, Liu and Libby [9,10] considered the role of variable density through the use of a similarity transformation. Both an infinitely fast reaction [9] and a detailed reaction set [10] were used to describe the oxidation of hydrogen to water. A single diffusion coefficient was assumed to reduce the numerical complexities. In the first case, the boundary layer was considered as an inner zone and an outer zone, where oxidant and fuel mass fractions

were close to zero and were contiguous at the flame sheet. For large rates of injection, the governing equations, which were in terms of flame sheet location, were solved by the application of asymptotic expansions with different boundary conditions for two different zones. The effective heat of formation of the product (H_2O) was modified to account for the creation of secondary products. The results showed good agreement with full equilibrium calculation. In the latter case, a quasilinearization was applied to solve the stiff boundary value-type differential equations and the authors reported

encountering numerical difficulties as the finite-rate chemical reaction rates increased. The limiting cases of frozen and equilibrium behavior are discussed.

Combustion and extinction phenomena in the forward stagnation region of a condensed fuel was studied experimentally and theoretically by Tien et al. [11]. In their numerical analysis, they assumed a second-order forward overall chemical reaction in gas phase, with gas-phase activation energy and modified frequency factor, determined by comparison with experimental results. The effect of external radiation on the extinction limit was also considered. Favorable agreement between experimental extinction data and theoretical prediction was obtained for a specified activiation energy and modified frequency factor.

Hahn, Wendt and Tyson [12] used a similar boundary layer approach to get the form of the equations in cylindrical coordinates. The conservation equations describing a flat laminar opposed-jet, moist CO, diffusion flame was solved by numerical integration. Prediction utilizing finite-rate, elementary combustion kinetics gave good agreement with a one-dimensional flame experiment.

Pellett et al. [18,19,20] conducted a series of opposed jet burner experiments to study the effect of air-contaminants on hydrogen diffusion flames. They observed a new phenomenon, which they named RESTORE. RESTORE is the opposite of extinction (or BLOWOFF) in the sense that the flame reestablishes itself at the axis. Their results show that the N_2-contaminated fuel has a more significant effect on the BLOWOFF than on the RESTORE condition and, like CO or CO_2 , each has moderately small but not negligible thermodynamic and chemical kinetic effects on the hydrogen diffusion flame in air. For the water-contaminated hydrogen diffusion flames, the results indicate that water will decrease the maximum sustainable H_2 mass flux, just prior to extinction, of a N_2-diluted, H_2-air diffusion flame.

The structure of several methane-air and hydrogen-nitrogen-oxygen counterflow diffusion flames were computed by Dixon-Lewis et al. [13]. They also used the boundary layer similarity solution and employed complex chemical reactions and detailed transport property calculations. Their effort is known to be the first to include detailed transport property calculations. They solved the momentum equation by a damped Newton method which runs in parallel with a time-dependent approach for the coupled energy and species equations. The extinction limits of both the methane-air and hydrogen-air flames at high velocity gradient were predicted and the freezing of the oxidant reactions on the fuel side of the hydrocarbon flames is discussed in terms of their chemical mechanism. Their results of methane-air flame agree well with the experimental data. However, the hydrogen-air flame experimental data available at that time (Pellett et al. [21]) were overlooked by the authors and, therefore, no comparisons were made with experiments.

III. MATHEMATICAL MODEL

The opposed-jet diffusion flame is considered to be an important configuration to obtain the kinetic data for highly reactive fuel-oxidant mixtures. Fig. 1 shows the geometry considered in the present analysis. We assume the flow is laminar everywhere. For nonreacting flow, the solution to this type of flow is given by the solution of two inviscid incompressible jets impinging on one another. However, the fuel contained in one jet will diffuse into the other jet and the oxidant will do likewise in the opposite direction, thus, establishing a narrow zone in which fuel and oxidant coexist. If the mixture is ignited, a thin flame surface will be established. The temperature will rise sharply at the flame. This narrow temperature peak will affect the density of the gases and the flow characteristics will now be different from those of the nonreacting flow. This flow must be determined from the solution of the equation of motion coupled with the equation of conservation of energy and species.

Because the effect of the flame on the flow field is restricted to a very narrow region, the problem can be considered as being similar to a boundary layer type flow, in which the viscous effects are restricted to a small region when compared to the entire flow field. This analogy, together with the assumption that the jets are infinitely wide compared with the zone of interest, suggests that equations representing the opposed jet diffusion flame may be converted into a set of ordinary differential equations with the use of a similarity transformation.

A. GOVERNING EQUATIONS

A complete description of system shown in Fig. 1 involves the simultaneous solution of the equations of conservation of momentum, energy and individual species.

The general equation of motion is

$$\rho \frac{D\vec{q}}{Dt} = -grad\, p + div\,(\mu\, grad\, \vec{q}) + B + \Psi \tag{1}$$

where ρ is the mixture density, D the substantial derivative, $\vec{q}$ the mass average velocity, t the time, p the pressure, μ the viscosity, B the body force, and Ψ stands for the viscous terms that are in addition to those expressed by $div\,(\mu\, grad\, \vec{q})$.

By applying the boundary-layer approach, the corresponding steady state momentum equation becomes

$$\rho u u_x + \rho v u_y = -p_x + (\mu u_y)_y \tag{2}$$

where u and v are the velocity components in the x and y directions and the subscripts x and y denote differentiation with respect to those independent variables.

The energy equation may be written for a moving element of fluid as

$$\rho\, \vec{q} \cdot grad \left(\sum c_i e_i\right) = div\,(\kappa\, grad\, T) - div \left(\sum \rho\, \vec{q}_i\, c_i\, h_i\right) - \sum \dot{w}_i''' h_i^{\circ} + p\, div\, \vec{q} + \Phi \tag{3}$$

where c_i, e_i, h_i, h_i° are, respectively, the mass fraction, the specific internal energy, enthalpy, and enthalpy of formation of species i, κ is the thermal conductivity, T is the temperature, $\dot{w}_i'''$ is the mass production rate of species i per unit volume, $\vec{q}_i$ is the diffusion velocity of species i with respect to $\vec{q}$, and Φ is the dissipation function.

Also, the species conservation equation for species i is given by i

$$div \left\{ \rho\, (\vec{q} + \vec{q}_i)\, c_i \right\} = \dot{w}_i''' \tag{4}$$

By combining Equations (3) and (4) with the auxiliary

relations

$$\sum \dot{w}_i''' = 0 \tag{5}$$

$$\sum \vec{q}_i c_i = 0 \tag{6}$$

$$\sum h_i = e_i + R_i T \tag{7}$$

where R_i is the gas constant for species i .

The steady state energy equation reduces to

$$\rho \vec{q} \cdot grad \left\{ \sum c_i \left(h_i + h_i^{\circ} \right) \right\} = div \left\{ \kappa \, grad \, T - \sum \rho \vec{q}_i c_i \left(h_i + h_i^{\circ} \right) \right\} + \vec{q} \cdot grad \, p + \Phi \tag{8}$$

With the general boundary layer assumption and expressions for diffusional velocity and mixture enthalpy given below

$$\vec{q}_i = -\left(D_i / c_i \right) grad \, c_i - \left(D_i^T / T \right) grad \, T \tag{9}$$

$$h = \sum c_i \left(h_i + h_i^{\circ} \right) \tag{10}$$

where D_i and D_i^T are, respectively, the molecular and thermal diffusion coefficient of species i , we see that Equation (8) becomes

$$\rho u h_x + \rho v h_y = \left(\kappa T_y \right)_y + u p_x + \mu (u_y)^2 + \left\{ \sum D_i \rho \left(h_i + h_i^{\circ} \right) c_{iy} \right\}_y + \left\{ \sum D_i^T \rho c_i \left(h_i + h_i^{\circ} \right) T_y / T \right\}_y \tag{11}$$

Noting that h_i is a function of temperature alone, we can have following expression from Equation (10)

$$grad\, h = \left\{\sum c_i\,(dh_i/dT)\right\} grad\, T + \sum\left(h_i + h_i^{\circ}\right) grad\, c_i \tag{12}$$

Let

$$\overline{c_p} = \sum c_i\,(dh_i/dT) = \sum c_i\, c_{pi} \tag{13}$$

We can combine Equation (2), (11) and (13) to obtain the desired steady state energy equation

$$\begin{aligned}
&\rho u\left(h + \frac{u^2}{2}\right)_x + \rho v\left(h + \frac{u^2}{2}\right)_y \\
&= \left\{(\kappa/\overline{c_p})\left(h + u^2/2\right)_y\right\}_y + \left\{(1/2)\left[\mu - (\kappa/\overline{c_p})\right]\left(u^2\right)_y\right\}_y \\
&+ \left\{\sum\left[D_i\rho - (\kappa/\overline{c_p})\right]\left(h_i + h_i^{\circ}\right)c_{iy}\right\}_y \\
&+ \left\{\sum\left(D_i^T\rho c_i/T\right)\left(h_i + h_i^{\circ}\right)T_y\right\}_y
\end{aligned} \tag{14}$$

For the species equation (4), we apply a similar boundary layer analysis and get

$$\rho u c_{ix} + \rho v c_{iy} = \left\{D_i\rho c_{iy} + D_i^T\rho c_i\, T_y/T\right\}_y + \dot{w}_i''' \tag{15}$$

For the velocity, v in the y direction, we introduce the general continuity equation

$$(\rho u x^n)_x + (\rho v x^n)_y = 0 \tag{16}$$

where $n = 0$ for two dimensional flow and 1 for axisymmetric flows.

Equations (2), (14), (15) and (16) thus constitute the system whose solution is required.

B. SIMILARITY TRANSFORMATION

As is usual in boundary layer problems, we seek solution of restricted form which permit reducing the original partial differential equations to ordinary differential form. In this problem, we assume that the boundary and initial conditions and the chemical behavior are such that velocity and enthalpy profiles remain similar to themselves along the stagnation plane, i.e., that all flow and gas parameters are functions of one coordinate η after the coordinate transformation. The procedure is as follows.

Let

$$\eta = \frac{\rho_e u_e x^n}{(2\xi)^{1/2}} \int_0^y \frac{\rho}{\rho_e} \, dy \tag{17}$$

and

$$\xi = \int_0^x \rho_e \mu_e u_e x^{2n} \, dx \tag{18}$$

where subscript e denotes the the edge of boundary layer.

If we substitute the potential flow solution near the stagnation point (i.e. $u_e = ax$) into the transformation, we get

$$\eta = \left\{ \frac{\rho_e a(n+1)}{\mu_e} \right\}^{\frac{1}{2}} \int_0^y \frac{\rho}{\rho_e} \, dy \tag{19}$$

and

$$\xi = \rho_e \mu_e a \frac{x^{2(n+1)}}{2(n+1)} \tag{20}$$

The coefficient a in the potential flow solution gives a measure of the characteristic time of the flow (Note that it has the dimension, 1/sec) and it depends on the flow geometry. The values of a for two dimensional and axisymmetric flow are [7]

$$a = u_e / \mathrm{d}\,, \qquad \text{for axisymmetric flow}$$

$$a = \pi \times u_e / 4H\,, \qquad \text{for two dimensional flow}$$

where d = diameter of the jet and H = width of the jet.

The transformation from x, y coordinates to ξ, η coordinates is carried out by means of the relations

$$\frac{\partial}{\partial y} = \frac{\rho u_e x^n}{(2\xi)^{1/2}} \frac{\partial}{\partial \eta} \tag{21}$$

$$\frac{\partial}{\partial x} = \rho_e \mu_e u_e x^{2n} \left[\frac{\partial}{\partial \xi} + \frac{\partial}{\partial \eta} \frac{\partial \eta}{\partial \xi} \right] \tag{22}$$

Introducing the stream function $\psi(\xi, \eta)$

$$\psi = (2\xi)^{1/2} f(\eta) \tag{23}$$

the overall continuity equation (16) is automatically satisfied by the usual relations

$$\rho u x^n = \frac{\partial \psi}{\partial y} \tag{24}$$

$$\rho v x^n = -\frac{\partial \psi}{\partial x} \tag{25}$$

In addition to Equations (21) – (24) and $u/u_e = f'(\eta)$, we choose the following dimensionless dependent variables

$$g = \frac{h}{h_e} \tag{26}$$

$$Y_i = \frac{c_i}{c_{i_e}} \tag{27}$$

$$\theta = \frac{T}{T_e} \tag{28}$$

The assumption that the kinetic energy $u^2/2 << h$

has been made and this term has been dropped from the energy equation.

By substituting into Equations (2), (14), (15) and (16) and removing the insignificant terms [Appendix A], we have the following similarity equations

$$\left(C f_{\eta\eta}\right)_\eta + f f_{\eta\eta} + \frac{1}{(n+1)}\left(\frac{\rho_e}{\rho} - f_\eta^{\,2}\right) = 0 \tag{29}$$

$$\left(\frac{C}{P_r}\, g_\eta\right)_\eta + f g_\eta + \left[\frac{C}{P_r}\sum \frac{c_{i_e} h_i}{h_e}\left\{(L_{e_i} - 1) Y_{i\eta} + \frac{L_{e_i}^T Y_i}{\theta}\frac{d\theta}{d\eta}\right\}\right]_\eta = 0 \tag{30}$$

$$\left(\frac{C}{P_r} L_{e_i} Y_{i\eta}\right)_\eta + f Y_\eta + \left(\frac{C}{P_r} \frac{L_{e_i}^T Y_i}{\theta} \frac{d\theta}{d\eta}\right)_\eta + \frac{1}{(n+1)a} \frac{\dot{w}_i'''}{\rho c_{i_e}} = 0 \qquad (31)$$

$$\rho v = -\rho_e \mu_e u_e x^n f / \sqrt{2\xi} \qquad (32)$$

where $C = \rho\mu/\rho_e\mu_e$, P_r is the Prandtl number ($\overline{c_p}\mu/\kappa$), L_{e_i} and $L_{e_i}^T$ are the Lewis number ($D_i\rho\overline{c_p}/\kappa$) and the thermal Lewis number ($D_i^T\rho\overline{c_p}/k$), respectively.

These equations, Equations (29) through (31), will be solved by the collocation method and time-marching finite difference technique. Equation (32) will be used to find normal velocity v.

C. BOUNDARY CONDITIONS

1. Momentum Equation. The momentum balance condition will be applied in the stagnation region. i.e.

$$\rho_{-\infty} u_{-\infty}^{\ 2} = \rho_\infty u_\infty^{\ 2}$$

Therefore

$$f_\eta(-\infty) = \frac{u_{-\infty}}{u_\infty} = \sqrt{\frac{\rho_\infty}{\rho_{-\infty}}} \qquad (33)$$

Other boundary conditions will be

$$f_\eta(\infty) = 1 \quad , \quad f(0) = 0 \qquad (34)$$

2. Energy Equation.

$$g(-\infty) = \sum g_{i,-\infty} Y_{i,-\infty} \quad , \qquad g(\infty) = \sum g_{i,\infty} Y_{i,\infty} \tag{35}$$

3. Species Equations.

$$Y_i(-\infty) = Y_{i,-\infty} \ , \ Y_i(\infty) = Y_{i,\infty} \tag{36}$$

D. THERMODYNAMIC AND TRANSPORT PROPERTIES

For the present analysis, the thermodynamic and transport property calculations are performed by the implementation of the CHEMKIN routines [14] and its extension [15]. The CHEMKIN routines provide the thermodynamic properties for the chemical species in terms of polynomial fits to the specific heat at constant pressure. Other thermodynamic properties are then given in terms of the fits to c_p. In the CHEMKIN routines, seven coefficients for two temperature ranges are used. These fits are given in the following form

$$\frac{c_{p_i}}{R_U} = a_{1\,i} + a_{2\,i}T + a_{3\,i}T^2 + a_{4\,i}T^3 + a_{5\,i}T^4 \tag{37}$$

where R_U is the universal gas constant. Since

$$\frac{h_i}{R_U} = \int_0^T c_{pi}\, dT$$

$$\frac{s_i}{R_U} = \int_0^T \frac{c_{pi}}{T}\, dT$$

where s_i is the entropy.

$$\frac{h_i}{R_U} T = a_{1\,i} + \frac{a_{2\,i}}{2} T + \frac{a_{3\,i}}{3} T^2 + \frac{a_{4\,i}}{4} T^3 + \frac{a_{5\,i}}{5} T^4 + \frac{a_{6\,i}}{T} \qquad (38)$$

$$\frac{s_i}{R_U} = a_{1\,i} \ln T + a_{2\,i} T + \frac{a_{3\,i}}{2} T^2 + \frac{a_{4\,i}}{3} T^3 + \frac{a_{5\,i}}{4} T^4 + a_{7\,i} \qquad (39)$$

where $a_{6,i}{}^* R_U$, $a_{7,i}{}^* R_U$ are, respectively, the enthalpy of formation and entropy at 0 K. Other thermodynamic properties can be easily calculated from $c_{p,i}$, h_i, and s_i.

The equations for the transport properties are given in Appendix B. A polynomial fit of the logarithm of the property to the logarithm of the temperature is chosen for the calculation. They are

$$\ln \mu_i = \sum_{k=1}^{4} b_{k\,i} (\ln T)^{k-1} \qquad (40)$$

The κ_i and D_{ki} can be expressed in a similar way. However, since the thermal diffusion ratios, Θ_i are only slightly dependent on temperature, we use polynomials in temperature, rather than the logarithm of temperature. i.e.

$$\ln \Theta_i = \sum_{k=1}^{4} b_{k\,i} T^{k-1} \qquad (41)$$

E. THE COMBUSTION MODEL

1. One Step Overal Combustion Model. A one-step, forward overall gas-phase chemical reaction is assumed for the combustion model. This simple chemical reaction system involves a reaction between two reactants (fuel and oxidant) in which they combine, in fixed proportions by mass, to produce a unique product.

$$\text{Fuel} + \text{Oxidant} \rightarrow \text{Product} \tag{42}$$

This model accords with reality with respect to the gross behavior, but suppresses the distracting intermediate details. The purpose of so doing is to generate quantitative predictions of combustion phenomena which are easy to perform and understand, which fit reality in its main features, and which can be refined when necessary. The following chemical reaction is considered for the hydrogen diffusion flame under this model.

$$H_2 + \frac{1}{2} O_2 \rightarrow H_2O \tag{43}$$

From this model, the production rate $\dot{w}_i'''$ in Equation (31) for hydrogen can be expressed as

$$\dot{w}_{H_2}''' = -Z_H \rho^2 Y_{H_2} Y_{O_2} \exp(-E_H/R_U T) \tag{44}$$

where Z_H is the reaction rate constant and E_H is the activation energy. Both Z_H and E_H are determined by comparing with experimental data.

In order to find the source terms for O_2 and H_2O , we introduce the equation of conservation of the production rate of all species

$$\sum_{i=1}^{ns} \gamma_{i\,m} \frac{\dot{w}_i'''}{M_i} = 0 \qquad (m = 1, 2, \ldots, l) \tag{45}$$

where $\gamma_{i\,m}$ is the number of atoms of the mth element in the ith species, M_i is the molecular weight of ith species, l is numbers of element in the reaction, and ns is the number of species.

From the one step combustion model, we have

$$\frac{\dot{w}_{H_2}'''}{M_{H_2}} + \frac{\dot{w}_{H_2O}'''}{M_{H_2O}} = 0 \tag{46}$$

$$\frac{\dot{w}_{H_2O}'''}{M_{H_2O}} + 2\frac{\dot{w}_{O_2}'''}{M_{O_2}} = 0 \tag{47}$$

These will be the production rates for H_2O and O_2.

2. Complete Reaction Mechanisms. An eleven reactions model is employed for detailed calculations. These reactions have been used successfully in the well-stirred reactor combustion simulation [24]. The general form for reversible (or irreversible) reactions can be represented by

$$\sum_{i=1}^{ns} \upsilon'_{im}\chi_i \rightleftarrows \sum_{i=1}^{ns} \upsilon''_{im}\chi_i \qquad (m = 1, 2, \ldots, nr) \tag{48}$$

where υ_{im} are stoichiometric coefficients, χ_i is the chemical symbol for ith species, and nr is the total number of reactions.

The production rate $\dot{w}_i'''$ can be written as a summation of the rate of progress variables for all nr reactions involving the ith species:

$$\dot{w}_i''' = \sum_{m=1}^{nr} \upsilon_{im} q_m \tag{49}$$

where $\upsilon_{im} = (\upsilon''_{im} - \upsilon'_{im})$

The rate of progress variable, q_m for the mth reaction is given by the difference of the forward rates and the reverse rates as

$$q_m = k_{f_m} \prod_{i=1}^{ns} [X_i]^{\upsilon'_{i\,m}} - k_{r_m} \prod_{i=1}^{ns} [X_i]^{\upsilon''_{i\,m}} \tag{50}$$

where $[X_i]$ is the mole concentration of the ith species and k_{f_m} and k_{r_m} are the forward and reverse rate constants of the mth reaction. They are equal to

$$k_{f_m} = A_m T^{\beta_m} \exp\left(-E_m / R_U T\right) \tag{51}$$

and

$$k_{r_m} = \frac{k_{f_m}}{k_{c_m}} \tag{52}$$

$$k_{c_m} = \exp\left(\sum_{i=1}^{ns} \chi_{i\,m} \frac{s_i}{R_U} - \sum_{i=1}^{ns} \chi_{i\,m} \frac{h_i}{R_U T}\right)\left(\frac{P_{atm}}{R_U T}\right)^{\sum_{i=1}^{ns} \chi_{i\,m}} \tag{53}$$

where the pre-exponential factor A_m, the temperature exponent β_m, and the activation energy E_m come from experiment and are given in Table I, P_{atm} denotes atmospheric pressure, and k_{c_m} is the equilibrium constant.

When a third body is needed for the reaction, the rate of progress variable is given by the equation below.

$$q_m = \left(\sum_{i=1}^{ns} \bar{\alpha}_{i\,m} [X_i]\right)\left(k_{f_m} \prod_{i=1}^{ns} [X_i]^{\upsilon'_{i\,m}} - k_{r_m} \prod_{i=1}^{ns} [X_i]^{\upsilon''_{i\,m}}\right) \tag{54}$$

If all species contribute equally as third bodies, then all $\bar{\alpha}_{i\,m} = 1$. However, it is often the case that some species act more efficiently as third bodies than do others. The $\bar{\alpha}_{i\,m}$ coefficients are then used to specify the increased efficiency of the ith species in the mth reaction.

Table I. CHEMICAL REACTION MECHANISMS FOR HYDROGEN-AIR DIFFUSION FLAME

	Chemical Reaction	A_m	β_m	E_m
1.	$H + O_2 \rightleftarrows O + OH$	5.1E+16	−0.82	16510.
2.	$H_2 + O \rightleftarrows H + OH$	1.8E+10	1.0	8830.
3.	$H_2 + OH \rightleftarrows H + H_2O$	1.2E+09	1.3	3630.
4.	$OH + OH \rightleftarrows O + H_2O$	6.0E+08	1.3	0.
5.	$H + OH + M \rightleftarrows H_2O + M$	7.5E+23	−2.6	0.
6.	$H_2 + M \rightleftarrows H + H + M$	2.2E+12	0.5	92600.
7.	$H + O_2 + M \rightleftarrows HO_2 + M$	2.1E+18	−1.0	0.
8.	$HO_2 + H \rightleftarrows H_2 + O_2$	2.5E+13	−0.0	700.
9.	$HO_2 + H \rightleftarrows OH + OH$	2.5E+14	−0.0	1900.
10.	$HO_2 + O \rightleftarrows OH + O_2$	4.8E+13	−0.0	1000.
11.	$HO_2 + OH \rightleftarrows H_2O + O_2$	5.0E+13	−0.0	1000.

For the numerical method implemented in this analysis, the production rates are divided into a creation rate and a destruction rate, i.e.,

$$\dot{w}_i''' = \dot{C}_i''' - \dot{D}_i''' \tag{55}$$

where

$$\dot{C}_i''' = \sum_{m=1}^{nr} \upsilon'_{i\,m}\, k_{r_m} \prod_{j=1}^{ns} [X_j]^{\upsilon''_{j\,m}} + \sum_{m=1}^{nr} \upsilon''_{i\,m}\, k_{f_m} \prod_{j=1}^{ns} [X_j]^{\upsilon'_{j\,m}} \tag{56}$$

$$\dot{D}_i''' = \sum_{m=1}^{nr} \upsilon'_{i\,m}\, k_{f_m} \prod_{j=1}^{ns} [X_j]^{\upsilon'_{j\,m}} + \sum_{m=1}^{nr} \upsilon''_{i\,m}\, k_{r_m} \prod_{j=1}^{ns} [X_j]^{\upsilon''_{j\,m}} \tag{57}$$

For third body reactions, similar to (54), each sum in the above equation is multiplied by the factor

$$\sum_{i=1}^{ns} \bar{\alpha}_{i\,m} [X_i]$$

These production rate calculations will be provided by the CHEMKIN routines.

3. The Damköhler Number. In the diffusion flame, the chemical reaction is generally faster than the species diffusion velocity, that is, the chemical reaction time is smaller than the diffusion time. Consequently, the chemical reaction occurs in a narrow region between the fuel and the oxidant; the concentrations of the reactants are very low in the reaction zone, and the combustion rate is controlled by the rate at which fuel and oxidant flow into the reaction zone.

Here, we introduce the Damköhler number which plays an important role in the prediction of extinction condition and in the interpretation of the numerical results. The definition for Damköhler number as proposed by Fendell [5] is

$$\begin{aligned} D_I &= \frac{\text{the characteristic flow time}}{\text{the characteristic chemical time}} \\ &= \frac{Z_H \rho_e}{a(n+1)} \end{aligned} \tag{58}$$

When D_I approaches zero, the flow becomes a frozen flow; if the Damköhler number approaches infinity, the flow is in chemical equilibrium. Within this semi-infinite range, 0 to ∞, the actual Damköhler number is determined by the finite chemical rate

calculation. Therefore, if the extinction of the diffusion flame occurs at a certain critical value of D_I for various combinations of fuel and oxidant, the characteristic chemical time, and accordingly the chemical rate can be estimated by measuring the flow time at flame extinction.

F. NUMERICAL ANALYSIS

1. The Collocation Method. The collocation package COLSYS was developed for solving mixed-order systems of multipoint boundary-value problems [16]. This is in contrast to several other codes which required conversion of a given problem to a first order system, thereby increasing the number of equations and changing the algebraic structure of the discretized problem. Numerous numerical experiments have demonstrated the stability of the collocation procedure, including adaptive mesh selection and error estimation. Therefore, this efficient package is chosen to solve the momentum equation with its boundary conditions (Eq.33 and 34).

The method of spline collocation at mesh points, as described in detail in Ref. 17, is implemented in COLSYS to solve the nonlinear differential equations. The problem is solved on a sequence of meshes with the solutions expressed in terms of a polynomial basis. After each iteration, the error is estimated to check against a user-prescribed tolerance. If deemed worthwhile, a redistribution of the mesh points is performed to roughly equidistribute the error to each subinterval and the solution is recomputed. If not, each subinterval is halved, a new solution is computed and the error is re-estimated. This iteration procedures will continue for linear problems until the error is within the tolerance. For nonlinear problems, the damped Newton's method of quasilinearization is performed. Thus, at each iteration a linearized equation is solved by the same collocation procedure as described above.

Since neither C nor ρ_e/ρ in Equation (29) varies significantly with mixture composition, Equation (29) is partially

uncoupled from the energy and species equations and it will be solved only after certain number of iterations to account for the effect of the similarity function f on the solution.

2. Time-Marching Technique. In order to employ the time dependent technique for the coupled set of energy and species equations, Equations (30) and (31) are replaced by the time-dependent form

$$\frac{1}{a}\frac{\partial g}{\partial t} = \left(\frac{C}{P_r} g_\eta\right)_\eta + f g_\eta + \left\{ \frac{C}{P_r} \sum c_{i_e} \frac{h_i}{h_e} \left[(L_{e_i} - 1) Y_{i\eta} + \frac{L_{e_i}^T Y_i}{\theta} \frac{d\theta}{d\eta} \right] \right\}_\eta \quad (59)$$

$$\frac{1}{a}\frac{\partial Y_i}{\partial t} = \left(\frac{C}{P_r} L_{e_i} Y_{i\eta}\right)_\eta + f Y_\eta + \left(\frac{C}{P_r} \frac{L_{e_i}^T Y_i}{\theta} \frac{d\theta}{d\eta}\right)_\eta + \frac{1}{(n+1)a} \frac{\dot{w}_i'''}{\rho c_{i_e}} \quad (60)$$

Because the concentration and temperature gradients are not uniform in the flow field, a continuously collapsing grid is required. The grid spacing is chosen to be fine toward the stagnation plane, where the gradients are much steeper. The collapsing factor, which is defined by $(\Delta\eta_{j+1} - \Delta\eta_j)/\Delta\eta_j$, should never exceed 10 percent to prevent the unsymmetrical truncation error accumulating rapidly. The finite difference algorithm is based on the control volume approach [25]. The control volume and the grid spacing distribution is shown in Fig. 3.

Equations (59) and (60) can be converted into the finite difference form through discretization. We use central differencing and upwind differencing methods for the diffusion term and the convection term, respectively, while the system of equations will be treated in a fully implicit manner with the exception of the source term for H_2O

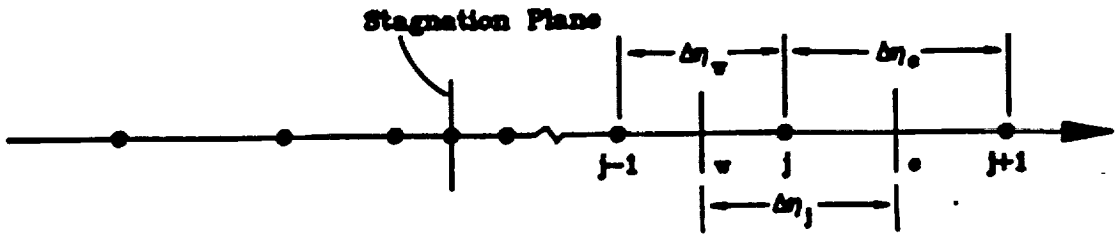

Figure 3. The Grid Spacing Distribution along η direction.

when the one-step combustion model is used. The equations can be expressed in the following form

$$E_{j-1}\, g_{j-1}^{t+1} + E_j\, g_j^{t+1} + E_{j+1}\, g_{j+1}^{t+1} = A \tag{61}$$

$$S_{i,j-1}\, Y_{i,j-1}^{t+1} + S_{i,j}\, Y_{i,j}^{t+1} + S_{i,j+1}\, Y_{i,j+1}^{t+1} = B_i \tag{62}$$

where :

$$E_{j-1} = -\left(\frac{C}{P_r\,\Delta\eta}\right)_w - \max[-f_w, 0.0]$$

$$E_{j+1} = -\left(\frac{C}{P_r\,\Delta\eta}\right)_e - \max[f_e, 0.0]$$

$$E_j = \Delta\eta_{j-1}\left(\frac{1}{a\Delta t} + f_j'\right) - E_{j-1} - E_{j+1} + (f_w - f_e)$$

where $\max[X, Y]$ denote the greater of X and Y

$$A = \Delta\eta_{j-1}\left(\frac{g_j^t}{a\,\Delta t} + \left[\frac{C}{P_r} \sum \frac{h_i}{h_e} \left\{ (L_{e_i} - 1) Y_{i\eta} + \frac{L_{e_i}^T Y_i}{\theta} \frac{d\theta}{d\eta} \right\} \right]_{\eta_j} \right)$$

$$S_{i,j-1} = -\left(\frac{C}{P_r} \frac{L_{e_i}}{\Delta\eta} \right)_w - \max[-(S_c)_w , 0.0]$$

$$S_{i,j+1} = -\left(\frac{C}{P_r} \frac{L_{e_i}}{\Delta\eta} \right)_e - \max[(S_c)_e , 0.0]$$

$$S_{i,j} = \Delta\eta_{j-1}\left(\frac{1}{a\Delta t} + f_j' + \dot{D}_{c_{i,j}} \right) - S_{i,j-1} - S_{i,j+1} + [(S_c)_w - (S_c)_e]$$

where

$$S_c = f + \frac{C}{P_r} \frac{L_{e_i}^T}{\theta} \frac{d\theta}{d\eta}$$

$$\begin{cases} \dot{D}_c = f_j' & \text{for } H_2O \text{ in the one-step model} \\ \dot{D}_c = f_j' + \dot{D}'''_i / Y_i & \text{otherwise} \end{cases}$$

$$B_i = \Delta\eta_{j-1}\left(\frac{Y_{i,j}^t}{a\,\Delta t} + \dot{C}_{c_{i,j}} \right)$$

where

$$\begin{cases} \dot{C}_c = 0.0 & \text{for } H_2 \text{ and } O_2 \text{ in the one-step model} \\ \dot{C}_c = \dot{C}'''_i & \text{otherwise} \end{cases}$$

Equations (61) and (62) constitute a (j-2) × (j-2) block tridiagonal matrix, where each block is a $ns \times ns$ matrix. This system will be solved by the Thomas Algorithm.

In order to compare the calculated normal velocity distribution with the experimental data, we need to find the physical normal coordinate that corresponds to η. From Equation (19) we have

$$\frac{d\eta}{dy} = \left\{ \frac{\rho_e a(n+1)}{\mu_e} \right\}^{\frac{1}{2}} \frac{\rho}{\rho_e}$$

or

$$\int_0^{\eta} \frac{\rho_e}{\rho} \, d\eta = \left\{ \frac{\rho_e a(n+1)}{\mu_e} \right\}^{\frac{1}{2}} \int_0^{y} dy \tag{63}$$

This gives us the relationship between η and y. The Romberg method will be used to perform the numerical integration of this equation.

For the global time-marching procedure, we start with initial guess profiles for both the temperature and the species mass fractions. A linear distribution with an assumed flame front as the peak point for both the profiles is chosen for this purpose. These initial profiles will then be smoothed by a commonly used curve-fitting routine. In order to find the coefficients appearing in the governing equations, The CHEMKIN routines are implemented and the same curve-fitting routine is used to find their derivatives. The momentum equation is, then solved by COLSYS to find the similarity parameter f. The equation of motion is partially decoupled from the energy and species equations, it will be solved after certain numbers of time steps to update the value of f. The time marching technique is implemented to find the enthalpy and species

distributions, which will be followed by a check for steady-state solutions. The criterion for testing for steady state solution is as follows.

$$| Y_i^{t+5} - Y_i^t | \leq \text{tolerance} \tag{64}$$

If these values are not within the specified tolerance a new temperature distribution will be calculated from the enthalpy using the interval-halving method and the coefficients will be updated and the procedure will be continued. Once Equation (64) is satisfied, the solution is assumed to have reached steady state and the normal velocity v is calculated from Equation (32). The solution obtained for one case will be used as the initial guesses for other cases; a series of solutions may be obtained in this manner, each time varying the parameters only slightly. This procedure greatly reduces computer time and effort involved in running a case.

IV. RESULTS AND DISCUSSION

A. THE EXPERIMENT

Several Opposed-Jet Burner (OJB) experiments were conducted by Pellett et al. [18, 19, 20, 21, 22] at the NASA Langley Research Center. The main experimental equipment included two, equal diameter, coaxial, circular tubes. Three different sets of OJB tubes were used, 2.7 mm, 5.0 mm and 7.0 mm i.d., respectively, in order to cover a wide range of conditions. The two OJB tubes were set in an aluminum mounting such that only axial adjustments in tube separation distance were permitted, while the radial movements were mechanically restricted. The burner was bathed in an argon atmosphere to prevent extraneous combustion outside the central impingement zone, which would hinder visibility of the flame. All measurement were made at atmospheric pressure and the reactants and tubes were maintained at room temperature throughout the measurements to preserve consistency in experimental conditions. A digital mass flow metering system was implemented to produce accurate flow rate for both tubes. The flow rates of fuel and air were adjusted such that the dish-shaped flame was centered between the two tubes. The flow was always laminar. Since the flow through the circular tubes is laminar at low Reynolds number, the velocity profile at the tube exit is parabolic.

When a laminar jet of nitrogen-diluted hydrogen was ejected from one tube and pure or contaminated air from the opposed tube, a counterflow flame was centered between the two tubes. For every specific hydrogen mole fraction measurement, the mass flowmeters were used to control this fixed rate. The respective jet flow velocities were increased slowly by adjusting the nitrogen-diluted hydrogen and air flows until extinction occurred, at which time the volume flow rates of hydrogen, nitrogen, and air were recorded. The flow velocities were then reduced in a similar way so that the

torus-shaped flame restored back to the jet axis. This abrupt restoration of the central flame is the so called RESTORE condition. The flow rate of each component was also recorded after RESTORE was established. In order to employ LDV technique to measure velocity distributions along the central axis, Al_3O_2-seeded air was used. After the specific flow condition was stabilized, the normal and radial velocities were recorded.

B. RESULTS

The present study was undertaken in order to understand the various aspects of hydrogen-air combustion such as the flame extinction characteristics. The presence of contaminants such as water vapor and carbon dioxide, the role of thermal diffusion of light species, and sensitivity to reaction mechanisms are some of the aspects considered to be important in this study. The development of an algorithm to solve a set of very stiff ordinary differential equations arising from the consideration of detailed chemical kinetics associated with the combustion of hydrogen was considered important because of the potential for the numerous studies that can be conducted to investigate the fundamental mechanisms concerning laminar and turbulent flames. These objectives have been accomplished in a two-step process; the first step involved the development of a one-step reaction model and the second step involved the development of a model with detailed chemistry consisting of 8 species and 22 reactions (counting both the forward and the backward reactions). The one-step reaction model proved to be very beneficial because it was possible to use the results from it as initial profiles for the detailed-chemistry model. Comparisons are made with the results obtained from these two models. The results are presented as temperature and species profiles and axial velocity profiles. The relative location of the flame with respect to the stagnation plane, flame thickness, the maximum values of temperature and species mass fractions and their relative locations are some of the items discussed in this

chapter. The results presented are only a representative sample to demonstrate the capabilities of the computer program rather than a set of detailed case studies. This approach was necessary because of the limitations of the size of, and turnaround time for the computers available at the University of Missouri-Rolla. The extinction conditions were obtained by making several runs and plotting the results on a temperature vs. strain rate (or the corresponding Damköhler number) plot. Extinction is defined as the condition where the temperature drops precipitously. All the profile plots are made with the stagnation point as the origin as shown in Fig 2. The plots are made in the physical coordinate rather than the transformed coordinate in order to facilitate comparison with experimental data.

Results from the one-step reaction model and the 8-species model are compared in Figs. 4, 5 and 6. Both these calculations were made at conditions corresponding flame extinction. Therefore, strain rates of 4500 s^{-1} and 7700 s^{-1}, respectively, were used for these two cases. Extinction is seen to take place at nearly the same peak temperature for the one-step model and the detailed chemistry model and flame thickness is not affected considerably by the choice of the chemistry model. However, the strain rate at extinction is higher (7700 s^{-1}) for the 8-species, 22-reaction model compared to the extinction strain rate of (4500 s^{-1}) for the single-step reaction model. The corresponding extinction strain rate from experiments is 4000 s^{-1}. It should be emphasized that the activation energy for the one-step model was chosen so that the strain rates for the experiment and the model match for one value of the mole fraction. Thus, the procedure for the one-step model should be thought of as a means of estimating the activation energy for the one-step reaction. The overprediction of the extinction strain rate by a factor of two by the 8-species model is probably due to the fact that the 'effective strain rate' at the flame is higher than the strain rate calculated from the cold flow velocity at the tube exit; this point has been discussed by Dixon-Lewis [13].

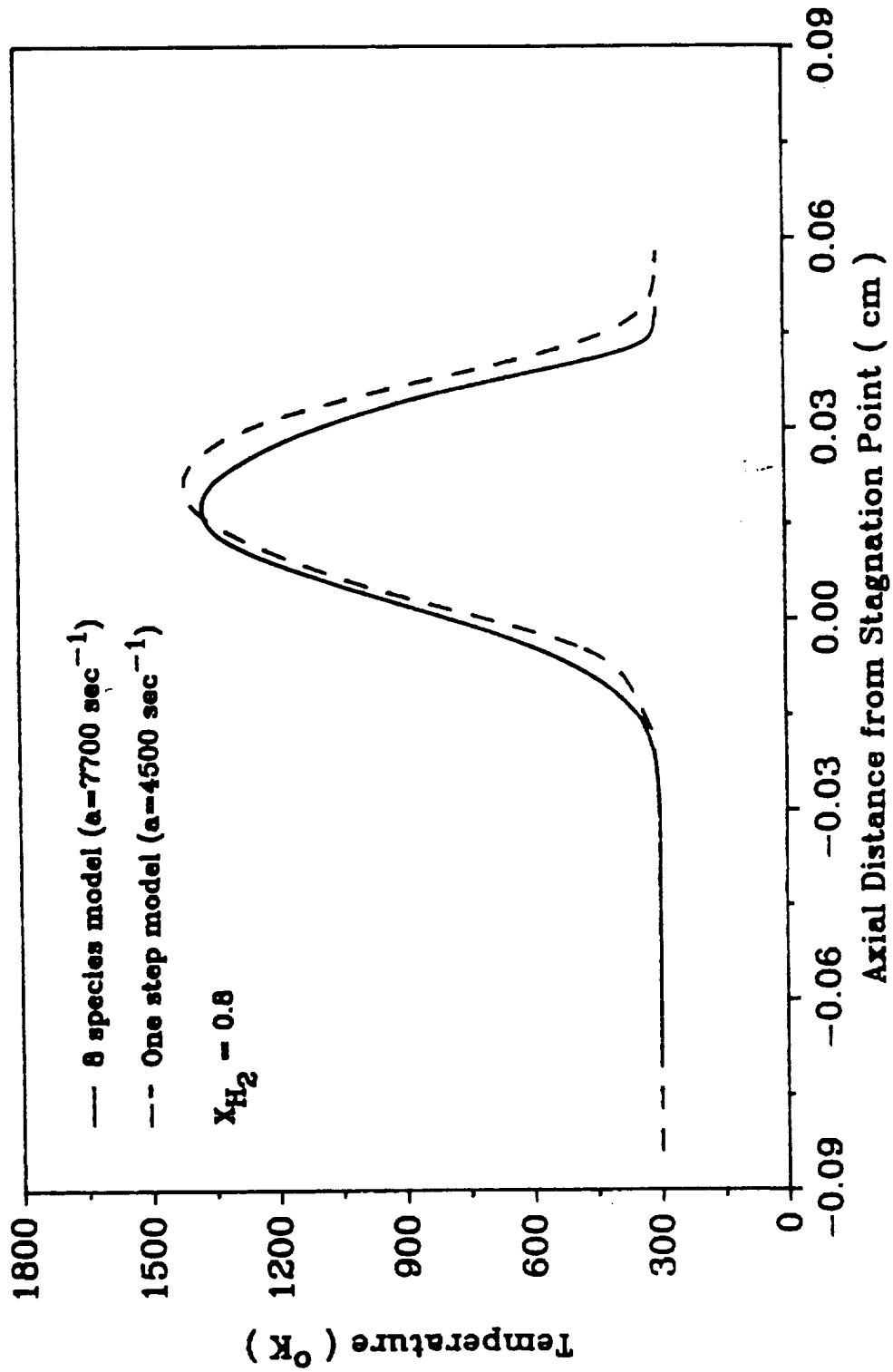

Figure 4. Temperature Comparison at Extinction between 8 Species and One-Step Models for $X_{H_2} = 0.8$.

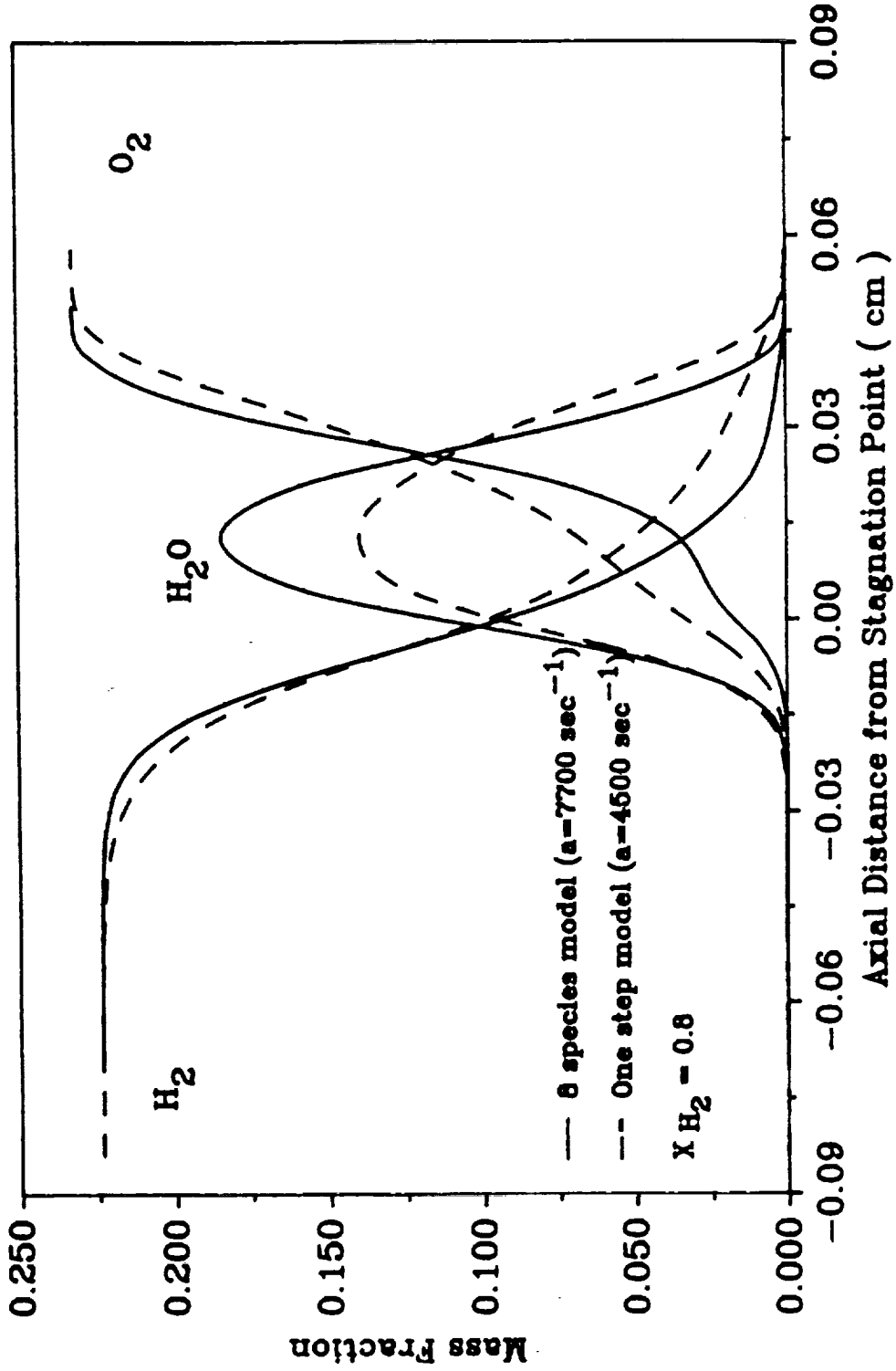

Figure 5. Major Species Mass Fraction Comparison at Extinction between 8 Species and One-Step Models for $X_{H_2} = 0.8$.

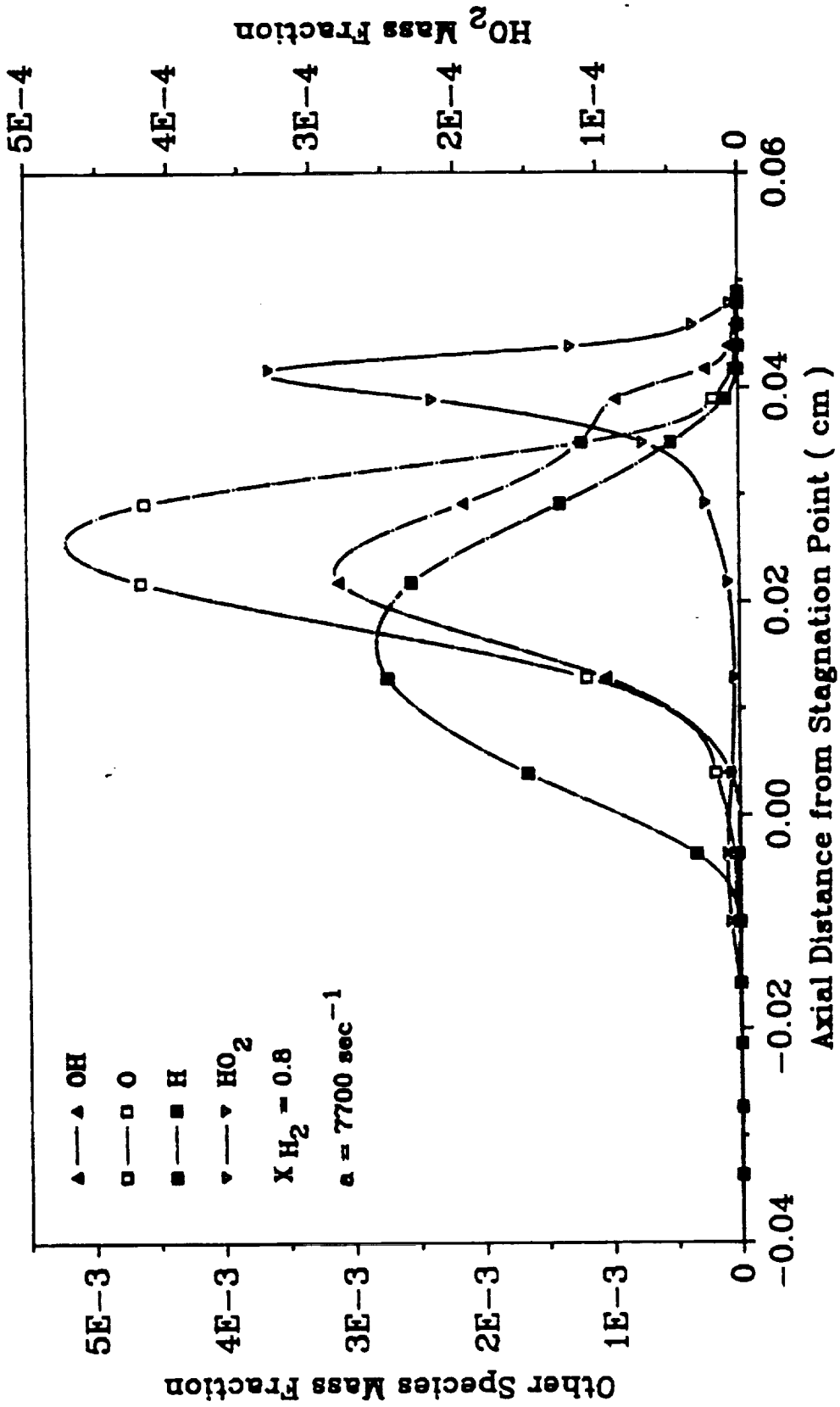

Figure 6. Minor Species Mass Fraction Distribution from 8 Species Model at Extinction for $X_{H_2} = 0.8$.

Flame location is an important parameter necessary to discuss flame characteristics. We may define flame location as the position of the peak temperature. Spalding [3] gave an analytical expression for the flame location from his flame sheet theory. Hahn, Wendt and Tyson [12] found it necessary to compromise flame location in order to compare experimental results and analysis. In the present study, the flame is located approximately 0.015 cm to the right of the stagnation plane, as can be seen in Fig. 4. The mass fraction profiles of the major species are shown in Fig. 5. The one-step model gives a peak H_2O mass fraction of about 0.14, whereas, the 8-species model gives a peak H_2O mass fraction of about 0.18. It may be noticed that the mass fraction peaks are to the left of the temperature peaks. The mass fraction profiles of minor species are shown in Fig. 6. The H-atom profile is seen to be rather flat extending from $y=0$ to $y=0.03$ cm. The HO_2 profile is distinct from the other profiles in that it shows two peaks to either side of the flame with their magnitudes much smaller compared to other minor species. Hahn, Wendt and Tyson [12] obtained analytical results which showed the flame to be thicker than the experimentally observed value for methane and CO counterflow diffusion flames. They also observed that the experimental reaction zone (as defined by the location of the peak temperature and that of intersection of reactant profiles) seemed to be shifted 0.25 cm to the fuel-lean side. Several probable factors that might have caused this difference in the flame location were identified by these authors; they subsequently adjusted their results to make the flame location from experiments and theory coincide.

The above comparisons indicate that the one-step reaction model gives useful information regarding several aspects of the flame. Computer runs with the one-step model take much less CPU time compared with the full-chemistry model. The full-chemistry model requires very careful preparation of initial profiles for obtaining successful steady-state solutions. For these reasons, the results presented hereafter are

based on the one-step model. These results could be used as guides for choosing cases to be run with the full chemistry model.

The variation of the maximum temperature as a function of the Damköhler number for various values of fuel mole fraction is plotted in Fig. 7. Each data point in this figure corresponds to one computer run. The extinction conditions from the experiments and analysis are presented in Fig. 8. This plot is obtained from the curves shown in Fig. 7. The plot shows the strain rates corresponding to various hydrogen mole fractions in the fuel stream. As stated earlier, the activation energy used in these calculations using the one-step reaction was chosen so that the results from experiments and analysis agree at hydrogen mole fraction equal to 0.6. This procedure was necessary because the activation energy for the one-step reaction model could not be determined satisfactorily using theory. It is worth mentioning that Tien, Singhal, Harrold and Prahl [11] have used a similar procedure to calculate extinction in the stagnation point boundary-layer of a condensed fuel using a one-step reaction model. The analytical curve in Fig. 7 has a larger slope compared to the experimental curve. The underlying reason for this behavior may be traced to the fact that the strain rates in this plot are obtained from cold flow at the pipe exit; the 'effective' strain rates may be larger than the ones obtained in this manner. The effective strain rate is likely to be a function of the heat release and, therefore, also the mole fraction of the fuel. This may be the reason why the analysis overpredicts the strain rates at higher mole fractions and underpredicts them at smaller mole fractions. It is, therefore, possible that improvements in the predictions could be obtained if the strain rates are corrected to account for the changes in the velocity profile due to heat release.

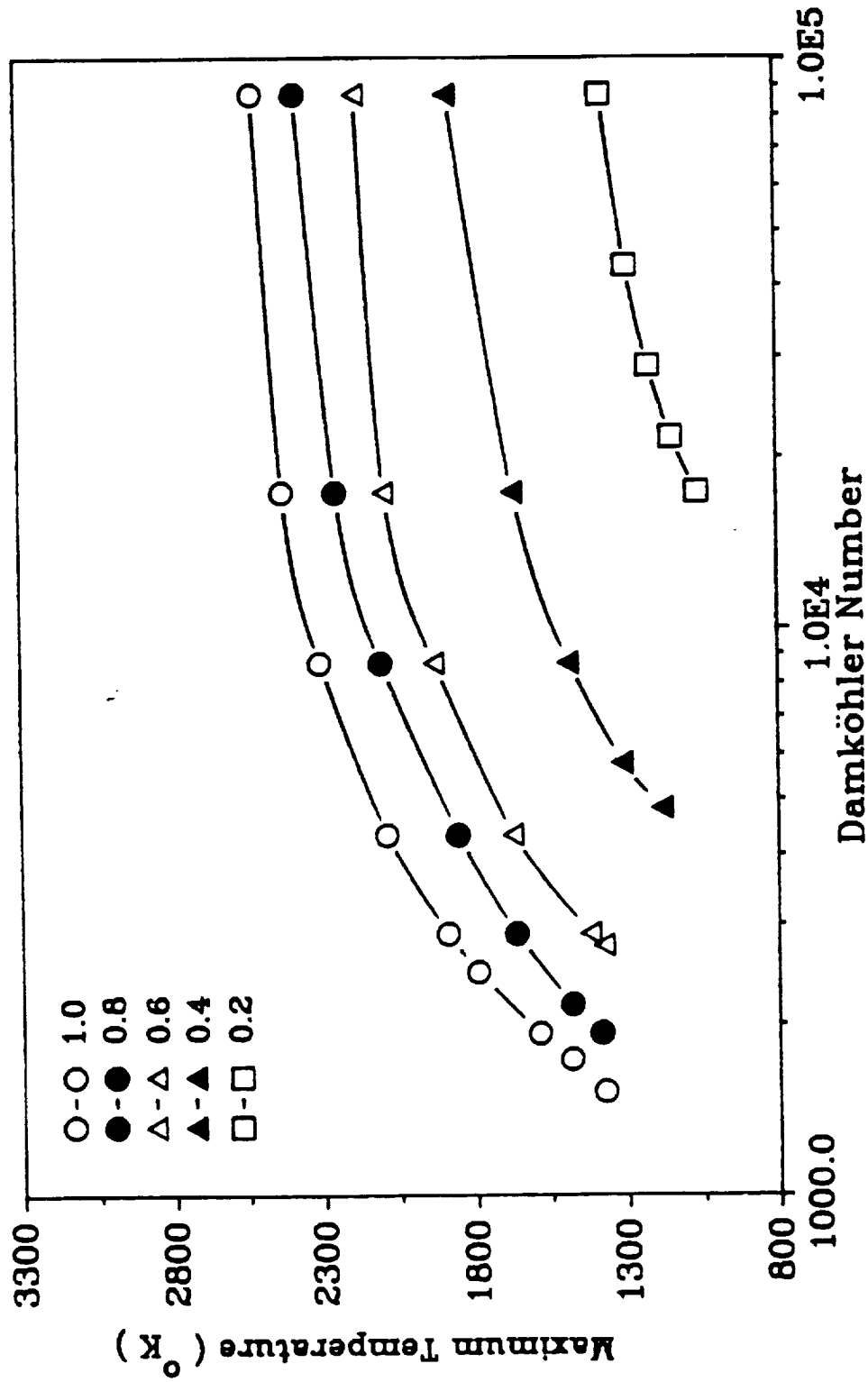

Figure 7. Flame Temperature vs. Damköhler Number for Various Hydrogen Mole Fractions.

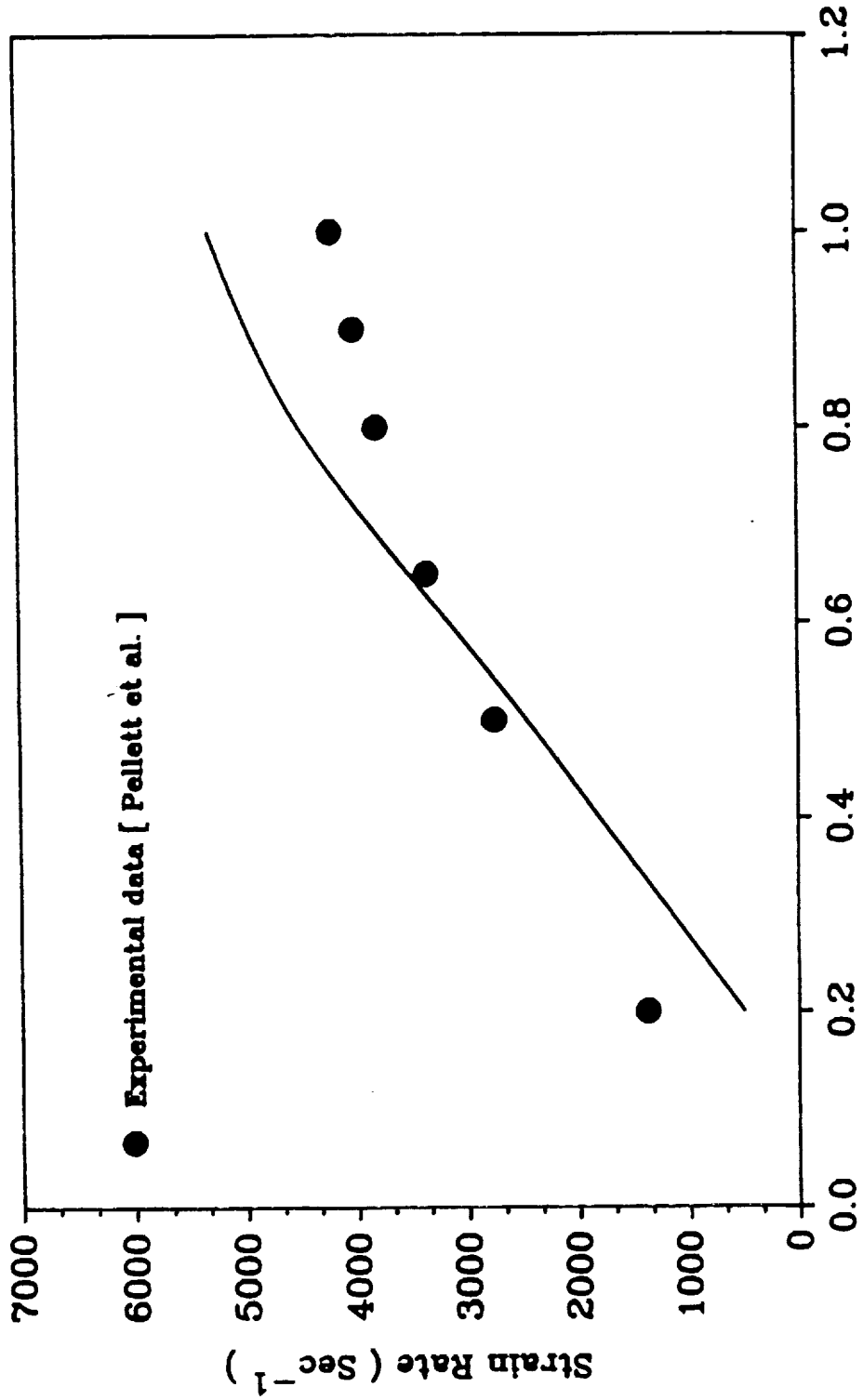

Figure 8. Extinction Limits Comparison between Experimental Data and One-Step Model.

Figs. 9, 10 and 11 show temperature profiles and mass fraction profiles for two extreme cases, one near equilibrium and the other near extinction. The equilibrium case has a thicker reaction zone because of the increased heat release. It should also be noted that the maximum temperature in this case is much higher that the near extinction case. Another feature to be observed in these figures is that the flame moves towards the stagnation plane as it approaches extinction. This sensitivity of the flame location with respect to the stagnation plane to the conditions under which the flame exists has been observed also by Dixon-Lewis et al. [13]. They observed that, in this regard, agreement for methane-air flame is much better than for hydrogen air flame. Pellett et al. [18-22] observed in their experiments that the flame becomes more planar and moves towards the fuel side as extinction is approached. This phenomenon is still not properly understood and no simple explanation exists for this behavior. It appears that the higher heat release in the hydrogen-air flame as compared with the methane-air flame does play a role in making the effect more pronounced in the former. Simply shifting the curve in order to match with experimental data, as was done in Ref. 12, does not appear to be satisfactory. Hahn et al.[12] attributed the discrepancy in flame location to factors such as inaccurate calculation of transport properties and/or kinetic parameters, incomplete chemical reaction mechanism, and the absence of buoyancy and radiation terms in the analytical model. The present results along with the observations of Dixon-Lewis et al. and Pellett et al. indicate that this phenomenon requires more careful attention for it to be completely explained.

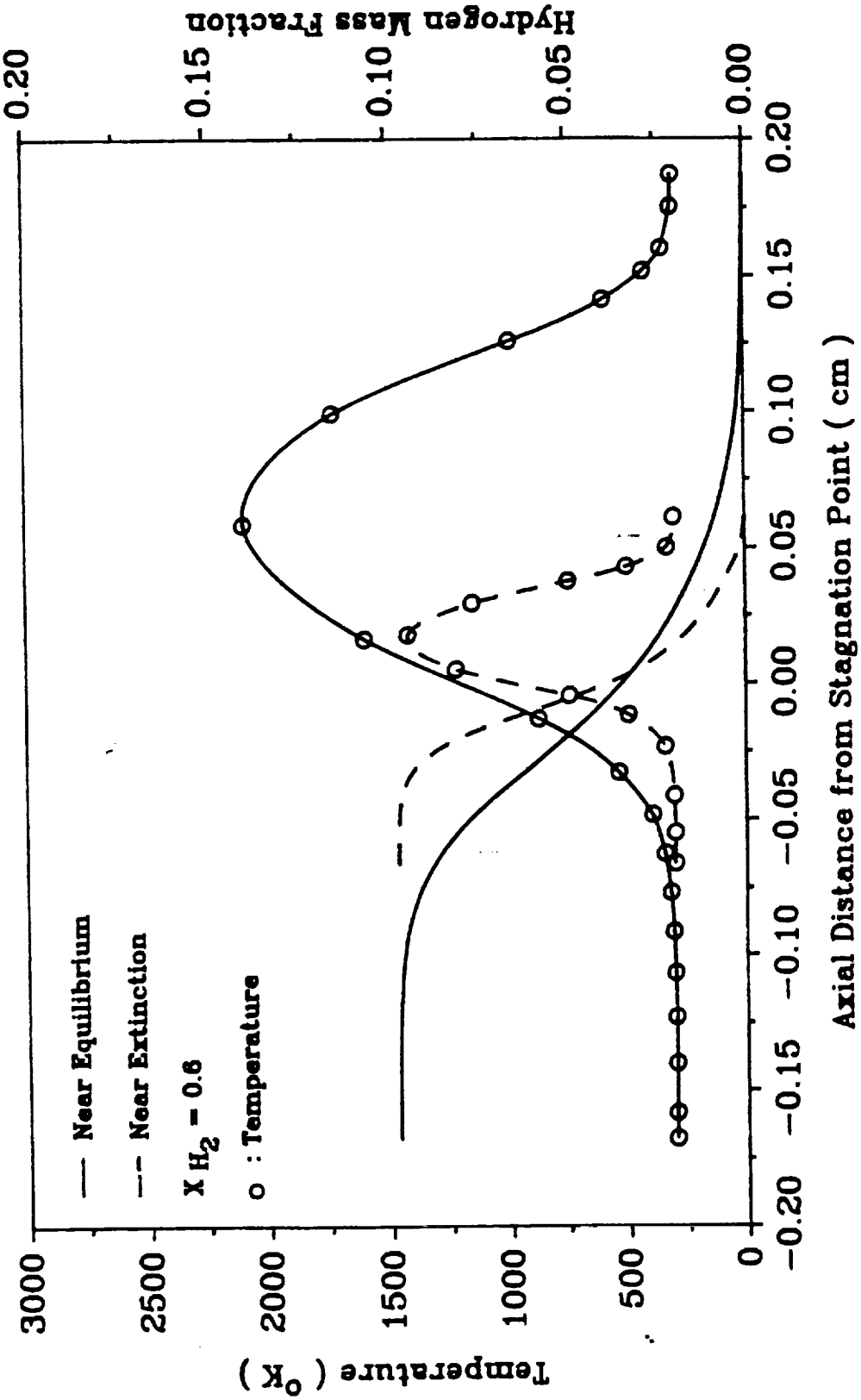

Figure 9. Comparison of Temperature and Hydrogen Profiles near Extinction and near Equilibrium for $X_{H_2} = 0.6$.

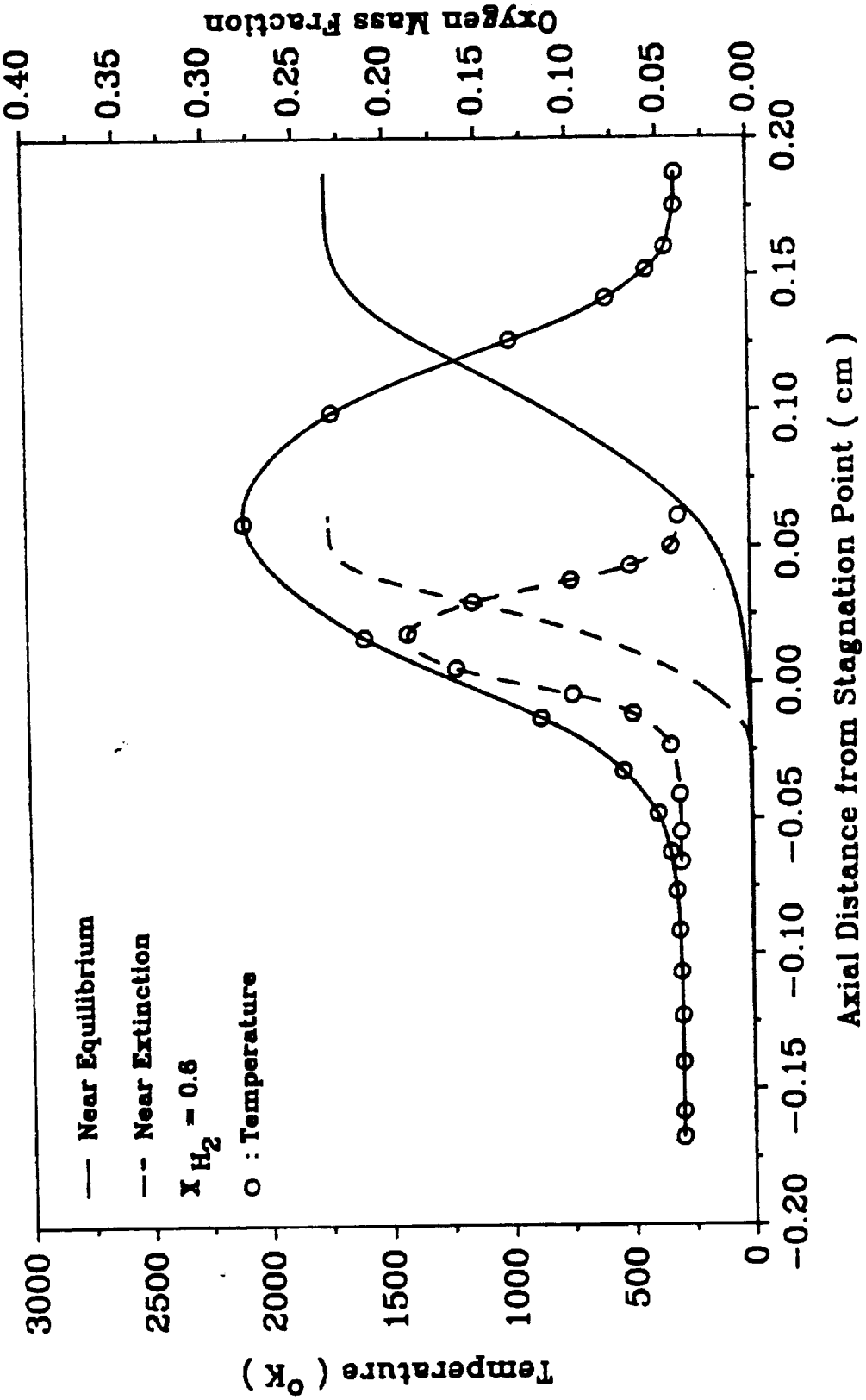

Figure 10. Comparison of Temperature and Oxygen Profiles near Extinction and near Equilibrium for $X_{H_2} = 0.6$.

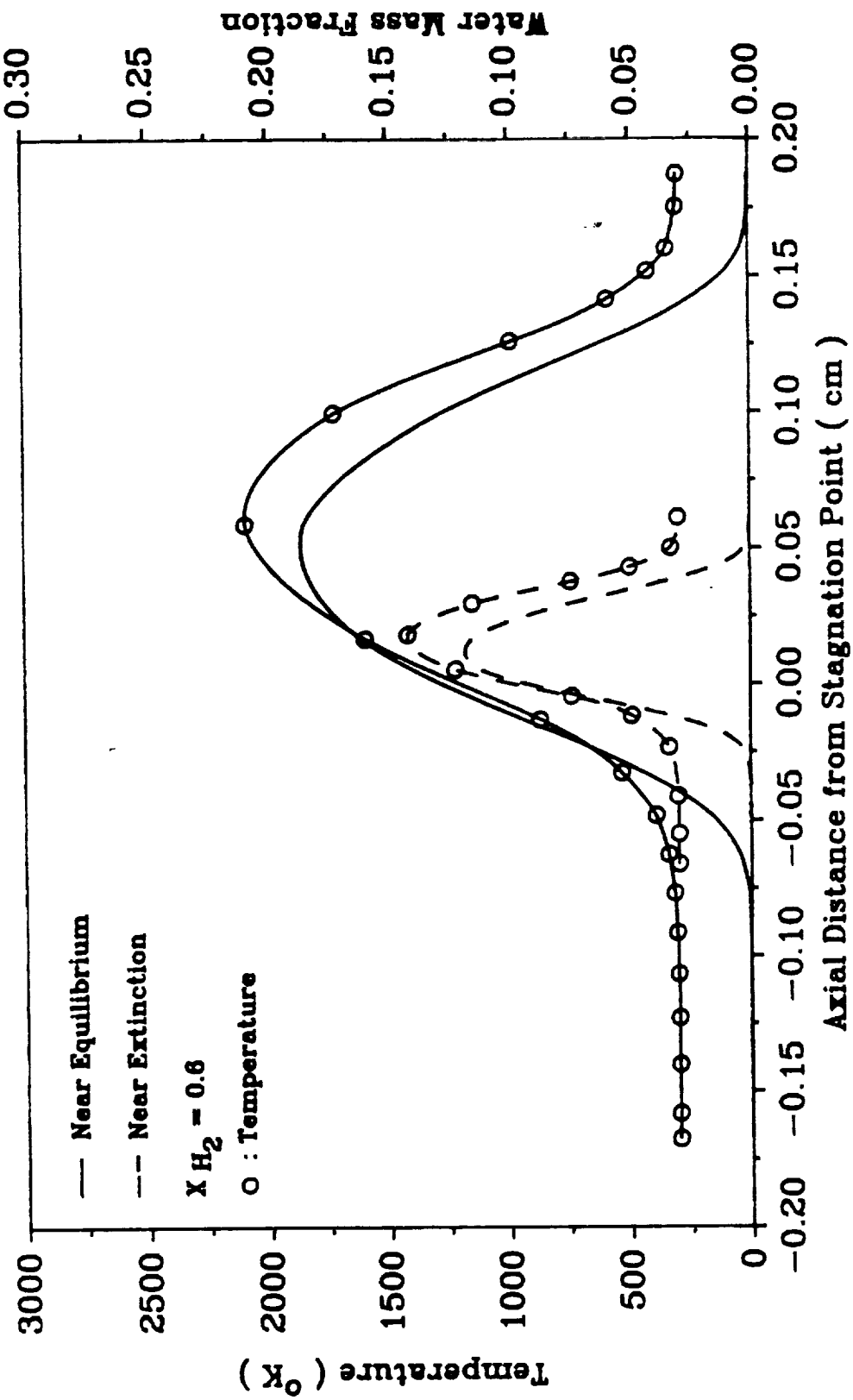

Figure 11. Comparison of Temperature and Water Profiles near Extinction and near Equilibrium for $X_{H_2} = 0.6$.

One concern that has arisen in the past regarding the use of hydrogen as the fuel is the role that thermal diffusion of light species such as H_2 and H has on the flame characteristics. A case study was, therefore, conducted to determine the extent to which thermal diffusion affects flame characteristics. The results are plotted in Figs. 12 and 13. These two figures demonstrate that thermal diffusion has little effect on the flame; its only influence appears to be a slight reduction in the peak temperature. It appears that using a more detailed model for thermal diffusion than the one presently used will not have any noticeable effects on the flame.

The experimental temperature profiles of Pellett et al. are compared with the predictions in Figs. 14 and 15. The experiments are based CARS (coherent antistokes Raman sepctroscopy) measurements. These figures and other results not shown here indicate the tendency to overpredict the temperature compared to experimental values. Hahn, Wendt and Tyson [12] and Dixon-Lewis et al. [13] also have reported overprediction of the temperature. Both these groups attributed the differences to the fact that no radiation correction was applied to the temperature measurements using thermocouples. However, the present results indicate that the discrepancies between experiments and analysis cannot be fully explained as being caused by thermal radiation because the temperature data used in the present study are based on CARS measurements. More work on the influence of grid distribution, number of species involved and the reaction set used for the calculations must be performed to answer this question. No direct measurement of the flame location with respect to the stagnation point was made in these experiments. Therefore, the differences in the flame location seen in Figs. 14 and 15 may not be realistic; the velocity profile plots give a more accurate picture of the flame location.

Finally, the experimental velocity profiles of Pellett et al. [22] are compared with the predictions in Figs. 16 and 17. The experimental data are based on LDV (laser-doppler velocimetry) measurements. The main feature to be observed in these two figures is the presence of the velocity maxima caused by heat release in the flame zone. Differences in the flame location between the experiments and the calculations persist in these figures. There is fairly good agreement in the magnitudes of the peak velocity.

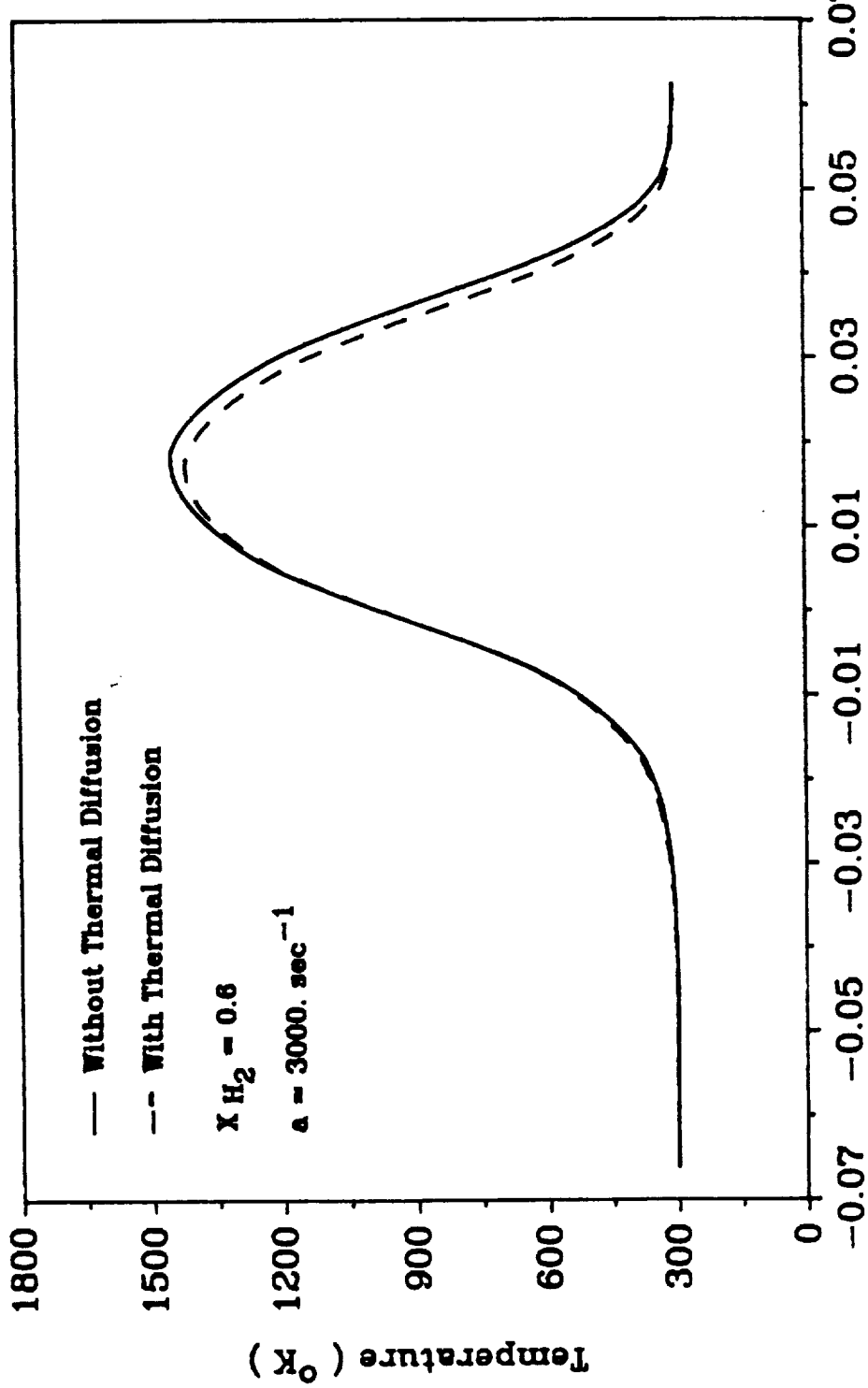

Figure 12. Effect of Thermal Diffusion on Temperature Distribution ($X_{H_2} = 0.6$, near extinction).

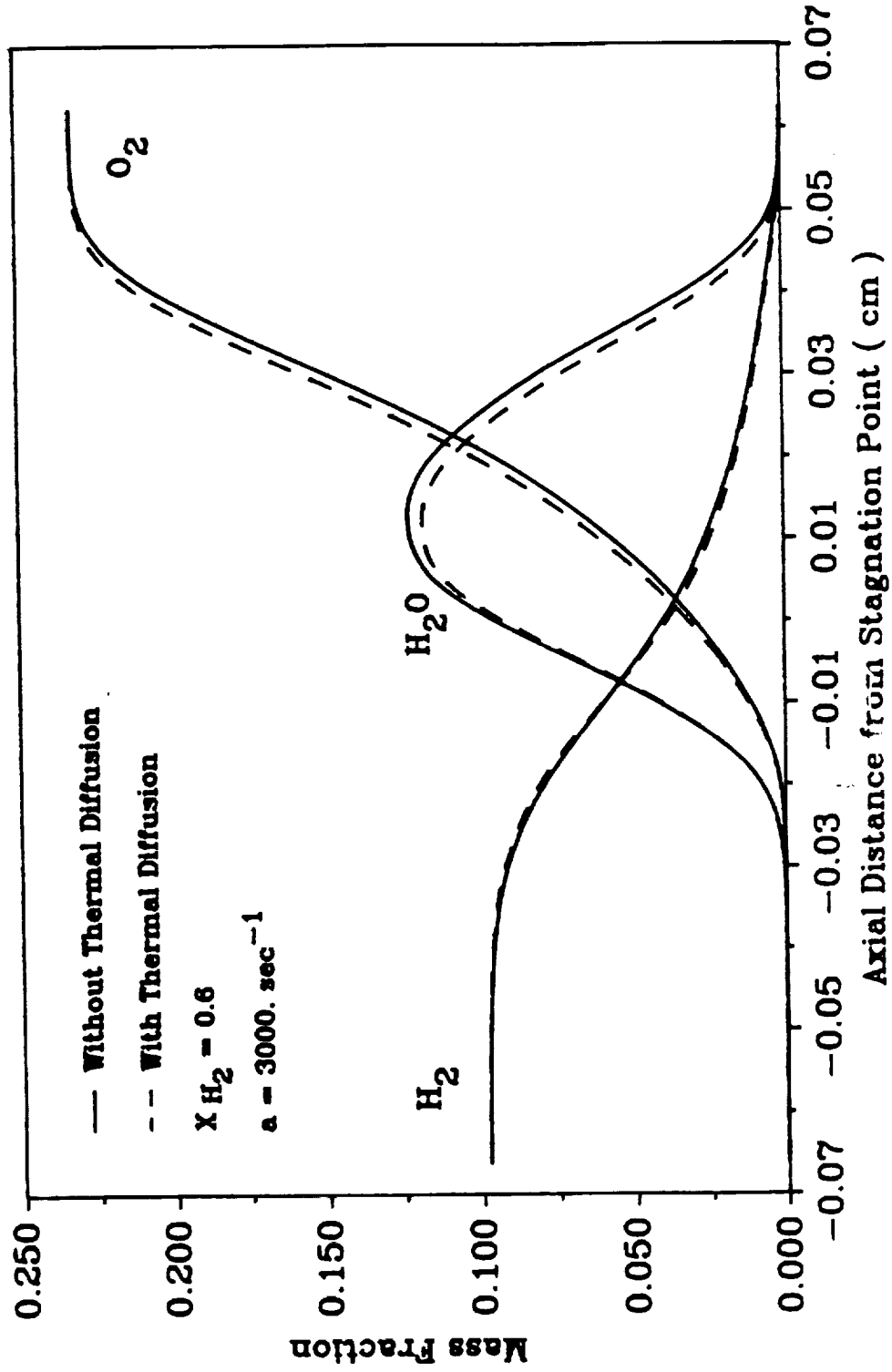

Figure 13. Effect of Thermal Diffusion on Species Distribution ($X_{H_2} = 0.6$, near extinction).

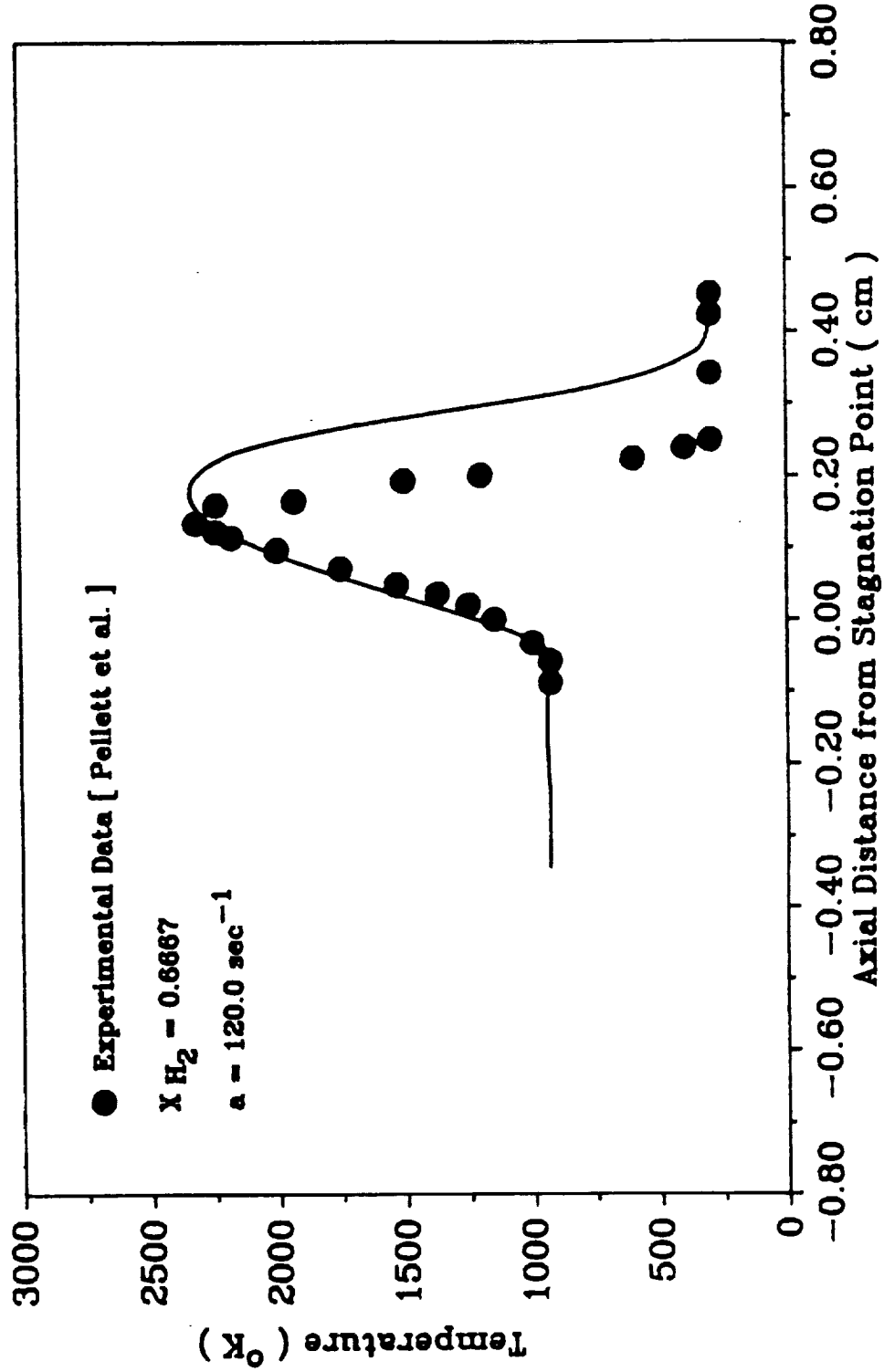

Figure 14. Comparison of Temperature Profiles from Experiments and Computations: a = 120 sec^{-1}, X_{H_2} = 0.6667.

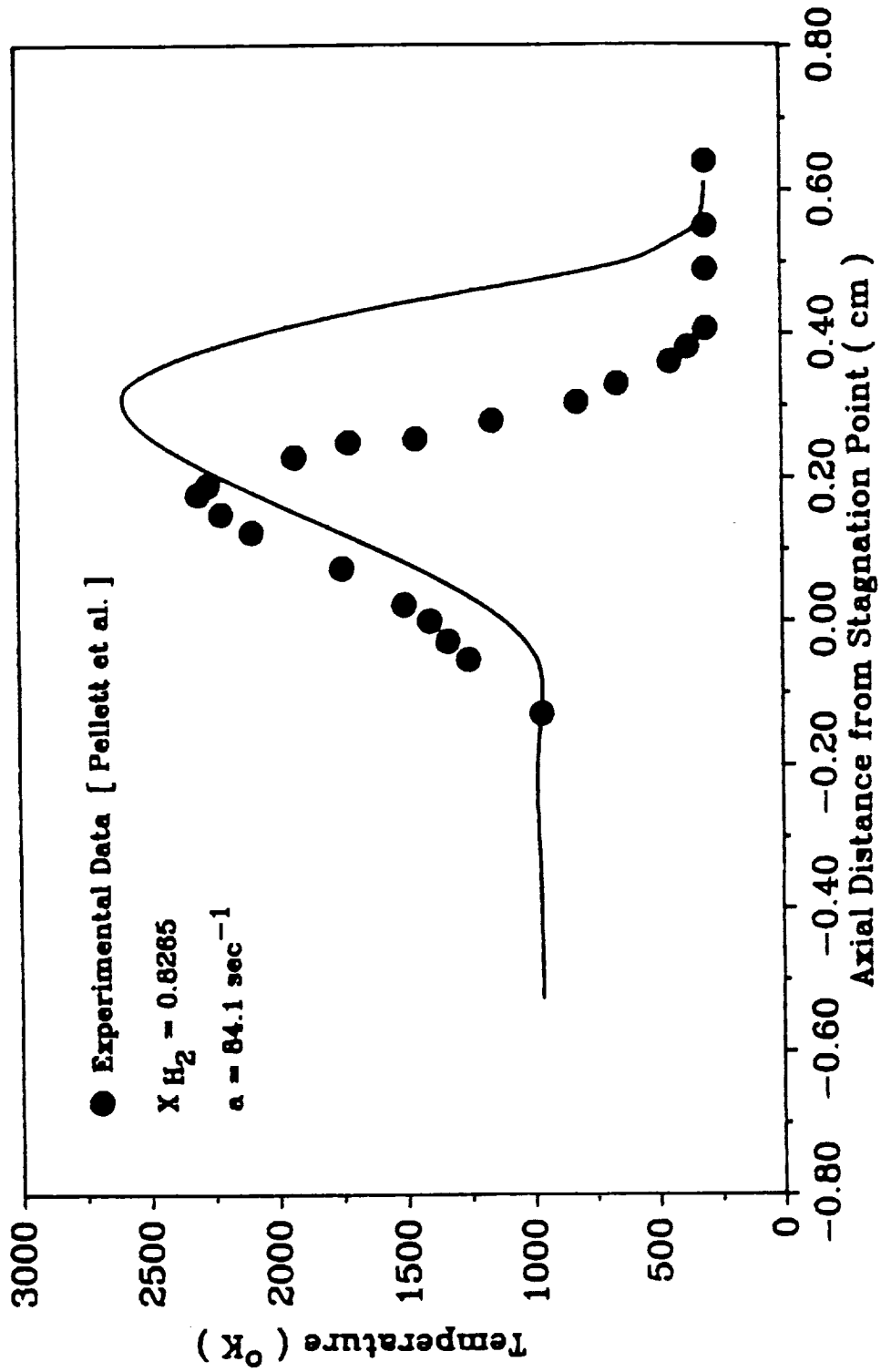

Figure 15. Comparison of Temperature Profiles from Experiments and Computations: a = 84.1 sec^{-1}, X_{H_2} = 0.8265.

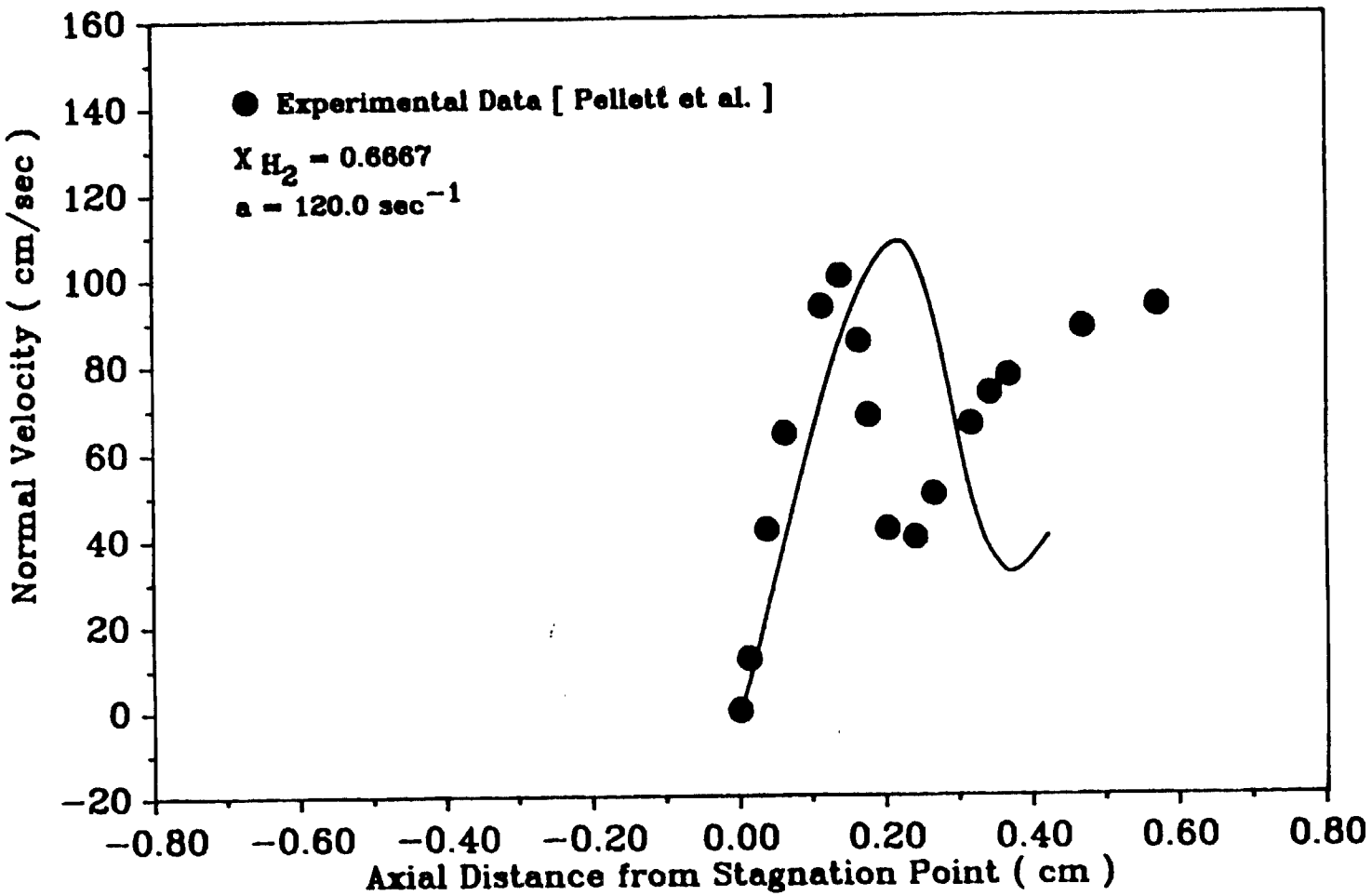

Figure 16. Comparison of Normal Velocity Profiles from Experiments and Computations: $a = 120$ sec $^{-1}$, $X_{H_2} = 0.6667$.

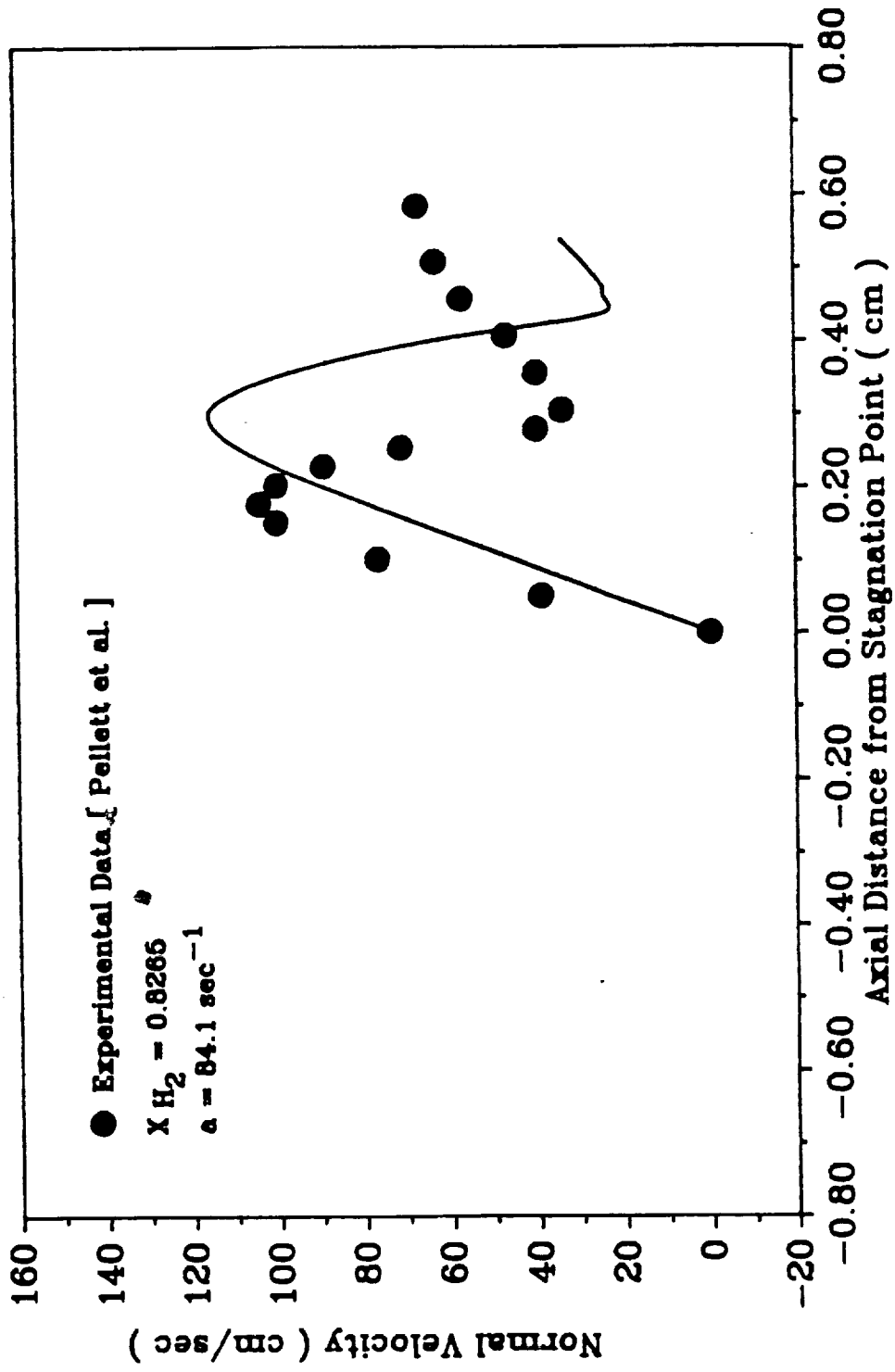

Figure 17. Comparison of Normal Velocity Profiles from Experiments and Computations: a = 84.1 sec^{-1}, X_{H_2} = 0.8265.

V. CONCLUSIONS

A capability has been developed to analyze counterflow diffusion flames. The ability to solve the stiff equations governing this problem when hydrogen is used as the fuel, is considered to be an important step in understanding the complex phenomena associated with counterflow diffusion flames. The numerical procedure based on the control volume approach with time-marching appears to be better suited to the present problem than the methods previously used for the solution of stiff ODEs. The present model uses detailed chemistry and accounts for variation of Prandtl number and Lewis number as well as considers the effect of thermal diffusion on the flame. It is shown that a one-step model can predict several features of the flame, while the detailed chemistry model can be used for fine tuning the results. The present results show that thermal diffusion has negligible effect on the characteristics of the flame. Further investigation is needed to settle some issues such as the flame location with respect to the stagnation plane, overprediction of the temperature by the analytical model and the considerable disagreement between theory and experiments on the extinction conditions; it is suggested that the actual strain rate in the flame zone, which is higher than the cold flow strain rate, must be the one to be considered for analyzing extinction.

Several valuable studies may be conducted using the present analytical model. The effect of contaminants on the flame is one such study currently being done. Consideration of more species such as H_2O_2 and more reactions could be used to understand the effect of the chemistry model on the flame. Use of the present model to investigate a recently proposed model for turbulent diffusion flames, according to which turbulent diffusion flames consist of a cluster of strained, laminar diffusion flamelets, will be an interesting and challenging task for investigators interested in turbulent diffusion flames.

BIBLIOGRAPHY

1. Potter, A.E. and Butler, J.N. "A Novel Combustion Measurement Based on the Extinguishment of Diffusion Flames", ARS Journal, Vol.29, 1954, pp. 54-56.

2. Potter, A.E., Heimel, S., and Butler, J.N. "Apparent Flame Strength: A Measure of Maximum Reaction Rate in Diffusion Flame", Eighth Symposium (International) on Combustion, 1962, pp. 1027-1034.

3. Spalding, D.B. "Theory of Mixing and Chemical Reaction in the Opposed Jet Diffusion Flame", ARS Journal, Vol.31, 1961, pp.763-771.

4. Anagnostou, E. and Potter, A.E. "Flame Strength of Propane-air Flames at Low pressure in Turbulent Flow", Ninth Symposium (International) on Combustion, Academic Press. New York, 1963, pp.1-6.

5. Fendell, F.E. "Ignition and Extinction on Combustion of Initially Unmixed Reactants", J. Fluid Mech., Vol.21, 1965, pp. 281-303.

6. Chung, P.M., Fendell, F.E., and Holt, J.E. "Non-Equilibrium Anomalies in the Development of Diffusion Flames", AIAA Journal, Vol.4, 1966, pp. 1020-1026.

7. Jain, V.K. and Mukunda, H.S. "On the Ignition and Extinction Problems in Forced Convection Systems", J. Heat Mass Transfer, Vol.11, 1968, pp. 491-508.

8. Jain, V.K. and Mukunda, H.S. "The Extinction Problem in an Opposed Jet Diffusion Flame with Competitive Reactions", Combustion Science and Technology, Vol.1, 1969, pp. 105-117.

9. Liu, T.M. and Libby, P.A. "Flame Sheet Model for Stagnation Points Flames", Combustion Science and Technology, Vol.2, 1971, pp. 377-388.

10. Liu, T.M. and Libby, P.A. "Boundary Layer at a Stagnation Point with Hydrogen Injection", Combustion Science and Technology, Vol.2, 1970, pp. 131-144.

11. T'ien, J.S., Singhal, S.N., Harrold, D.P., and Prahl, J.M. "Combustion and Extinction in the Stagnation-Point Boundary Layer of a Condensed Fuel", Combustion and Flame, Vol.33, 1978, pp. 55-68.

12. Hahn, W.A., Wendt, J.O.L., and Tyson, T.J. "Analysis of the Flat Laminar Opposed Jet Diffusion Flame with Finite Rate Detailed Chemical Kinetics", Combustion Science and Technology, Vol.27, 1981, pp. 1-17.

13. Dixon-Lewis, G., David, T., and Gaskell, P.H. "Structure and Properties of Methane-air and Hydrogen-air Counterflow Diffusion Flames", Archivum Combustions, Vol.6, No.1, 1986, pp. 3-21.

14. Kee, R.J., Miller, J.A., and Jefferson T.H. "CHEMKIN: A General-Purpose, Problem-Independent, Transportable, Fortran Chemical Kinetics Code Package", Sandia National Laboratories Report, SAND80-8003, 1980.

15. Kee, R.J., Warnatz, J., and Miller, J.A. "A FORTRAN Computer Code Package for the Evaluation of Gas-Phase Viscosities, Conductivities, and Diffusion Coefficients", Sandia National Laboratories Report, SAND83-8209, 1983.

16. Ascher, U., Christiansen J., and Russell, R.D. "COLSYS: Collocation Software for Boundary-Value ODEs", ACM Trans. on Mathematical Software, Vol.7, No.2, 1981, pp. 209-222.

17. Ascher, U., Christiansen J., and Russell, R.D. "A Collocation Solver for Mixed Order Systems of Boundary Value Problems", Mathematics of Computation, Vol.33, 1979, pp. 659-679.

18. Pellett, G.L., Jentzen, M.E., Wilson, L.G., and Northam, G.B. "Effects of Water-Contaminated Air on Blowoff Limits of Opposed Jet Hydrogen-Air Diffusion Flames", AIAA Preprint No. AIAA-88-3295 10 pp., 1988.

19. Guerra, R., Pellett, G.L., Wilson, L.G., and Northam, G.B. "Opposed Jet Burner Studies of Effects of CO, CO_2, and N_2 Air-Contaminants on Hydrogen-Air Diffusion Flames", AIAA Preprint No. AIAA-87-1960 14 pp., 1987.

20. Guerra, R., Pellett, G.L., Wilson, L.G., and Northam, G.B. "Opposed Jet Burner Studies of Hydrogen Combustion with Pure and N_2, NO Contaminanted Air" , AIAA Preprint No. AIAA-87-0090 11 pp., 1987.

21. Pellett, G.L., Northam, G.B.,Guerra, R., and Wilson, L.G. "Opposed Jet Burner Studies of Silane-Methane, Silane-Hydrogen, and Hydrogen Diffusion Flames with Air", CPIA Publication 457, Vol.1, 1986, pp. 391-404.

22. Pellett, G.L., Northam, G.B.,Guerra, R., Wilson, L.G., Jarrett Jr., O., Antcliff, R.R., Dancey, C.L., and J.A. Wang "Opposed Jet Diffusion Flames of Nitrogen-Diluted Hydrogen vs Air: Axial LDA and CARS Surveys; Fuel/Air Strain Rates at Extinction", AIAA Preprint No. AIAA-89-2522, 19 pp. 1989.

23. Fay, J.A. and Riddell, F.R. "Theory of Stagnation Point Heat Transfer in Dissociated Air", J. Aeronautical Sciences, Vol.25, 1958, pp. 73-85.

24. Glarborg, P., Kee, R.J., Grcar, J.F., and Miller, J.A. "PSR: A Fortran Program for Modeling Well-Stirred Reactors", Sandia National Laboratories Report, SAND86-8209, 1986.

25. Patankar, S.V. "Numerical Heat Transfer and Fluid Flow", Hemisphere, Washington D.C., 1980.

26. Hirschfelder, J.O., Curtiss, C.F., and Bird, R.B., "Molecular Theory of Gases and Liquids", John Wiley and Sons, Inc., New York, 1954.

27. Monchick, L. and Mason, E.A., "Transport Properties of Polar Gases", J. Chem. Phys., 35, pp. 1676, 1961.

28. Warnatz, J., "Influence of Transport Models and Boundary Conditions on Flame Structure", Numerical Methods in Flame Propagation, Eds. N. Peters and J. Warnatz, Friedr. Vieweg and Sohn, Wiesbaden, 1982.

29. Marrero, T.R. and Mason, E.A., "Gaseous Diffusion Coefficients", J. Phys. Chem. Ref. Dat., 1, pp. 3, 1972.

30. Chapman, S. and Cowling, T.G., "The Mathematical Theory of Non-Uniform Gases', Third Edition, Cambridge University Press, Cambridge, 1970.

APPENDIX A

DERIVATION OF THE SIMILARITY TRANSFORMATION EQUATIONS

We will outline here the detailed derivation of Equation (29) through (32). For convenience, we rewrite the operators (21), (22), and introduce a more general expression for stream function

$$\frac{\partial}{\partial y} = \frac{\rho u_e x^n}{(2\xi)^{1/2}} \frac{\partial}{\partial \eta} \tag{21}$$

$$\frac{\partial}{\partial x} = \rho_e \mu_e u_e x^{2n} \left[\frac{\partial}{\partial \xi} + \frac{\partial}{\partial \eta} \frac{\partial \eta}{\partial \xi} \right] \tag{22}$$

$$\psi = (2\xi)^{1/2} f(\xi, \eta) \tag{A.1}$$

A. NORMAL VELOCITY

The equation for normal velocity is

$$\rho v x^n = -\frac{\partial \psi}{\partial x} \tag{25}$$

From Equation (22) and $u/u_e = \partial f/\partial \eta$, we have

$$\begin{aligned} \frac{\partial \psi}{\partial x} &= \sqrt{2\xi}\, \rho_e \mu_e u_e x^{2n} \left(f_\xi + f_\eta \eta_\xi \right) + \rho_e \mu_e u_e x^{2n} f/\sqrt{2\xi} \\ &= \rho_e \mu_e u_e x^{2n} \left(\sqrt{2\xi}\, f_\xi + \sqrt{2\xi}\, f_\eta \eta_\xi + f/\sqrt{2\xi} \right) \end{aligned} \tag{A.2}$$

Then, from Equation (25)

$$\begin{aligned} \rho v &= -x^{-n} \frac{\partial \psi}{\partial x} \\ &= -\rho_e \mu_e u_e x^n \left(\sqrt{2\xi}\, f_\xi + \sqrt{2\xi}\, f_\eta \eta_\xi + f/\sqrt{2\xi} \right) \end{aligned} \tag{A.3}$$

If $f=f(\eta)$ is the case, we neglect those derivatives with respect to ξ

$$\rho v = -\rho_e \mu_e u_e x^n f/\sqrt{2\xi} \tag{32}$$

B. MOMENTUM EQUATION

The equation of motion is

$$\rho u u_x + \rho v u_y = -p_x + (\mu u_y)_y \tag{2}$$

From Equation (21) and (22), we have

$$\frac{\partial u}{\partial x} = \rho_e \mu_e u_e^2 x^{2n} \left(f_{\xi\eta} + f_{\eta\eta}\,\eta_\xi\right) + \rho_e \mu_e u_e x^{2n} f_\eta\, u_{e_\xi} \tag{A.4}$$

$$\frac{\partial u}{\partial y} = \frac{\rho u_e^2 x^n}{\sqrt{2\xi}} f_{\eta\eta} \tag{A.5}$$

$$\begin{aligned}\frac{\partial(\mu u_y)}{\partial y} &= \frac{\rho u_e x^n}{\sqrt{2\xi}} \left(\rho\mu \frac{u_e^2 x^n}{\sqrt{2\xi}} f_{\eta\eta}\right)_\eta \\ &= \frac{\rho u_e^3 x^{2n}}{2\xi} \left(\rho_e \mu_e \frac{\rho\mu}{\rho_e \mu_e} f_{\eta\eta}\right)_\eta \\ &= \rho_e \mu_e \frac{\rho u_e^3 x^{2n}}{2\,\xi} (C f_{\eta\eta})_\eta\end{aligned} \tag{A.6}$$

The first term on LHS of Equation (2) becomes

$$\begin{aligned}\rho u u_x &= \rho u_e f_\eta \left[\rho_e \mu_e u_e^2 x^{2n} \left(f_{\xi\eta} + f_{\eta\eta}\,\eta_\xi\right) + \rho_e \mu_e u_e x^{2n} f_\eta\, u_{e_\xi}\right] \\ &= \rho_e \mu_e \rho u_e^3 x^{2n} f_\eta \left(f_{\xi\eta} + f_{\eta\eta}\,\eta_\xi\right) + \rho_e \mu_e \rho u_e^2 x^{2n} f_\eta{}^2 u_{e_\xi}\end{aligned} \tag{A.7}$$

Combining Equation (A.3) and (A.5), the second term on the LHS is

$$\rho v u_y = -\rho_e \mu_e \rho u_e^3 x^{2n} \left(f_\xi + f/2\xi + f_\eta \eta_\xi \right) f_{\eta\eta} \tag{A.8}$$

$$\begin{aligned} \frac{\partial p}{\partial x} &= -\rho_e u_e \frac{du_e}{dx} \\ &= -\rho_e^2 \mu_e u_e^2 x^{2n} \frac{du_e}{d\xi} \end{aligned} \tag{A.9}$$

Dividing each term by $\rho_e \mu_e \rho u_e^3 x^{2n}/2\xi$, we get the following momentum equation

$$\left(C f_{\eta\eta}\right)_\eta + f f_{\eta\eta} + \frac{2\xi}{u_e} \frac{du_e}{d\xi} \left(\frac{\rho_e}{\rho} - f_\eta^{\,2} \right) = 2\xi \left(f_\eta f_{\eta\xi} - f_\xi f_{\eta\eta} \right) \tag{A.10}$$

For $f = f(\eta)$ and $u_e = ax$, we have the final momentum equation.

$$\left(C f_{\eta\eta}\right)_\eta + f f_{\eta\eta} + \frac{1}{(n+1)} \left(\frac{\rho_e}{\rho} - f_\eta^{\,2} \right) = 0 \tag{29}$$

C. ENERGY EQUATION

The energy equation (14) is

$$\begin{aligned} &\rho u \left(h + \frac{u^2}{2} \right)_x + \rho v \left(h + \frac{u^2}{2} \right)_y \\ &= \left\{ (\kappa/\overline{c_p}) \left(h + u^2/2 \right)_y \right\}_y + \left\{ (1/2) \left[\mu - (\kappa/\overline{c_p}) \right] \left(u^2 \right)_y \right\}_y \\ &+ \left\{ \sum \left[D_i \rho - (\kappa/\overline{c_p}) \right] \left(h_i + \dot{h_i} \right) c_{iy} \right\}_y \\ &+ \left\{ \sum \left(D_i^T \rho c_i / T \right) \left(h_i + \dot{h_i} \right) T_y \right\}_y \end{aligned} \tag{14}$$

We can have following relations from Equation (21) and (22)

$$\frac{\partial(h + u^2/2)}{\partial x} = \rho_e \mu_e u_e x^{2n} h_e (g_\xi + g_\eta \eta_\xi) \tag{A.11}$$

$$\frac{\partial(h + u^2/2)}{\partial y} = \frac{\rho u_e x^n}{\sqrt{2\xi}} h_e g_\eta \tag{A.12}$$

$$\frac{\partial c_i}{\partial y} = \frac{\rho u_e x^n}{\sqrt{2\xi}} c_{i,e} Y_{i,\eta} \tag{A.13}$$

$$\frac{\partial T}{\partial y} = \frac{\rho u_e x^n}{\sqrt{2\xi}} T_e \theta_\eta \tag{A.14}$$

$$\frac{\partial(u^2)}{\partial y} = 2u \frac{\partial u}{\partial y} = 2u_e^2 f_\eta \frac{\rho u_e x^n}{\sqrt{2\xi}} f_{\eta\eta} \tag{A.15}$$

The first term on LHS becomes

$$\rho u(h + u^2/2)_x = \rho_e \mu_e \rho u_e^2 x^{2n} h_e f_\eta (g_\xi + g_\eta \eta_\xi) \tag{A.16}$$

With Equation (A.3), the second term on LHS is

$$\begin{aligned} &\rho v(h + u^2/2)_y \\ &= -\rho_e \mu_e u_e x^n \left(\sqrt{2\xi} f_\xi + \sqrt{2\xi} f_\eta \eta_\xi + f/\sqrt{2\xi}\right) \frac{\rho u_e x^n}{\sqrt{2\xi}} h_e g_\eta \\ &= -\rho_e \mu_e \rho u_e^2 x^{2n} h_e \left(f_\xi g_\eta + g_\eta f/2\xi + f_\eta g_\eta \eta_\xi\right) \end{aligned} \tag{A.17}$$

Similarly, the terms on the RHS become

$$\begin{aligned}\left\{\left(\frac{\kappa}{\overline{c_p}}\right)(h + u^2/2)_y\right\}_y &= \frac{\rho u_e x^n}{\sqrt{2\xi}}\left\{\left(\frac{\kappa}{\overline{c_p}}\right)\frac{\rho u_e x^n}{\sqrt{2\xi}} h_e g_\eta\right\}_\eta \\ &= \frac{\rho_e\mu_e\rho u_e^2 x^{2n} h_e}{2\xi}\left\{\left(\frac{\kappa}{\overline{c_p}\mu}\right)\frac{\rho\mu}{\rho_e\mu_e} g_\eta\right\}_\eta \\ &= \frac{\rho_e\mu_e\rho u_e^2 x^{2n} h_e}{2\xi}\left\{\frac{C}{P_r} g_\eta\right\}_\eta\end{aligned} \tag{A.18}$$

$$\begin{aligned}&\left\{\left(\frac{1}{2}\right)\left[\mu - \left(\frac{\kappa}{\overline{c_p}}\right)\right](u^2)_y\right\}_y \\ &= \frac{\rho u_e x^n}{\sqrt{2\xi}}\left\{\frac{1}{2}\left[\mu - \frac{\kappa}{\overline{c_p}}\right]2u_e^2\frac{\rho u_e x^n}{\sqrt{2\xi}} f_\eta f_{\eta\eta}\right\}_\eta \\ &= \frac{\rho_e\mu_e\rho u_e^4 x^{2n}}{2\xi}\left\{\left(\frac{\rho\mu}{\rho_e\mu_e} - \frac{\rho\mu}{\rho_e\mu_e}\frac{\kappa}{\overline{c_p}\mu}\right) f_\eta f_{\eta\eta}\right\}_\eta \\ &= \frac{\rho_e\mu_e\rho u_e^4 x^{2n}}{2\xi}\left\{\left(1 - \frac{1}{P_r}\right) C f_\eta f_{\eta\eta}\right\}_\eta\end{aligned} \tag{A.19}$$

$$\begin{aligned}&\left\{\sum[D_i\rho - (\kappa/\overline{c_p})]\left(h_i + \mathring{h}_i\right)c_{iy}\right\}_y \\ &= \frac{\rho u_e x^n}{\sqrt{2\xi}}\left\{\sum[D_i\rho - (\kappa/\overline{c_p})]\left(h_i + \mathring{h}_i\right)\frac{\rho u_e x^n}{\sqrt{2\xi}} c_{i,e} Y_{i\eta}\right\}_\eta \\ &= \frac{\rho_e\mu_e\rho u_e^2 x^{2n}}{2\xi}\left\{\sum\frac{\rho\mu}{\rho_e\mu_e}\frac{\kappa}{\overline{c_p}\mu}\left[\frac{D_i\rho\overline{c_p}}{\kappa} - 1\right]c_{i,e} Y_{i\eta}\left(h_i + \mathring{h}_i\right)\right\}_\eta \\ &= \frac{\rho_e\mu_e\rho u_e^2 x^{2n}}{2\xi}\left\{\left(\frac{C}{P_r}\right)\sum c_{i,e}\left(h_i + \mathring{h}_i\right)(L_{e_i} - 1)Y_{i\eta}\right\}_\eta\end{aligned} \tag{A.20}$$

$$
\begin{aligned}
&\left\{\sum (D_i^T \rho c_i / T)(h_i + h_i^\circ) T_y\right\}_y \\
&= \frac{\rho u_e x^n}{\sqrt{2\xi}} \left\{\sum (D_i^T \rho c_i / T)(h_i + h_i^\circ) \frac{\rho u_e x^n}{\sqrt{2\xi}} T_e \theta_\eta\right\}_\eta \\
&= \frac{\rho_e \mu_e \rho u_e^2 x^{2n}}{2\xi} \left\{\sum \frac{\rho\mu}{\rho_e \mu_e} \frac{\kappa}{\overline{c_p}\mu} (h_i + h_i^\circ) \frac{D_i^T \rho \overline{c_p}}{\kappa} c_{i,e} Y_i \frac{\theta_\eta}{\theta}\right\}_\eta \\
&= \frac{\rho_e \mu_e \rho u_e^2 x^{2n}}{2\xi} \left\{\left(\frac{C}{P_r}\right) \sum c_{i,e} (h_i + h_i^\circ) L_{e_i}^T Y_i \frac{\theta_\eta}{\theta}\right\}_\eta
\end{aligned}
\tag{A.21}
$$

Dividing each term by $\rho_e \mu_e \rho u_e^2 x^{2n} h_e / 2\xi$, we get the following energy equation

$$
\begin{aligned}
&\left(\frac{C}{P_r} g_\eta\right)_\eta + f g_\eta + \left[\frac{C}{P_r} \sum \frac{c_{i,e} h_i}{h_e} \left\{(L_{e_i} - 1) Y_{i\eta} + \frac{L_{e_i}^T Y_i}{\theta} \frac{d\theta}{d\eta}\right\}\right]_\eta \\
&+ (u_e^2 / h_e)\left\{(1 - P_r^{-1}) C f_\eta f_{\eta\eta}\right\}_\eta = 2\xi (f_\eta g_\xi - f_\xi g_\eta)
\end{aligned}
\tag{A.22}
$$

If we assume $u_e^2 << h_e$ and neglect derivatives with respect to ξ, we have Equation (30).

$$
\left(\frac{C}{P_r} g_\eta\right)_\eta + f g_\eta + \left[\frac{C}{P_r} \sum \frac{c_{i,e} h_i}{h_e} \left\{(L_{e_i} - 1) Y_{i\eta} + \frac{L_{e_i}^T Y_i}{\theta} \frac{d\theta}{d\eta}\right\}\right]_\eta = 0 \tag{30}
$$

D. SPECIES EQUATIONS

The boundary layer species equation is

$$
\rho u c_{ix} + \rho v c_{iy} = \left\{D_i \rho c_{iy} + D_i^T \rho c_i T_y / T\right\}_y + \dot{w}_i''' \tag{15}
$$

From Equation (21), we find

$$\frac{\partial c_i}{\partial x} = \rho_e \mu_e u_e x^{2n} c_{i,e} \left(Y_{i\xi} + Y_{i\eta} \eta_\xi \right) \tag{A.23}$$

The first term on LHS of Equation (15) becomes

$$\begin{aligned} \rho u c_{ix} &= \rho u_e f_\eta \rho_e \mu_e u_e x^{2n} c_{i,e} \left(Y_{i\xi} + Y_{i\eta} \eta_\xi \right) \\ &= \rho_e \mu_e \rho u_e^2 x^{2n} c_{i,e} \left(Y_{i\xi} + Y_{i\eta} \eta_\xi \right) \end{aligned} \tag{A.24}$$

Combining Equation (A.13) and (A.5), the second term on the LHS is

$$\rho v c_{iy} = -\rho_e \mu_e \rho u_e^2 x^{2n} c_{i,e} \left(f_\xi + f/2\xi + f_\eta \eta_\xi \right) Y_{i\eta} \tag{A.25}$$

The first term on the RHS becomes

$$\begin{aligned} &\left\{ D_i \rho c_{iy} + D_i^T \rho c_i T_y / T \right\}_y \\ &= \frac{\rho u_e x^n}{\sqrt{2\xi}} \left\{ D_i \frac{\rho u_e x^n}{\sqrt{2\xi}} c_{i,e} Y_{i\eta} + D_i^T \rho c_{i,e} \frac{\rho u_e x^n}{\sqrt{2\xi}} \frac{\theta_\eta}{\theta} \right\}_\eta \\ &= \frac{\rho u_e^2 x^{2n}}{2\xi} c_{i,e} \left\{ \frac{\kappa}{\overline{c_p}} \left[\left(\frac{D_i \rho \overline{c_p}}{\kappa} \right) \rho Y_{i\eta} + \frac{D_i^T \rho \overline{c_p}}{\kappa} \rho Y_i \frac{\theta_\eta}{\theta} \right] \right\}_\eta \\ &= \frac{\rho u_e^2 x^{2n}}{2\xi} c_{i,e} \rho_e \mu_e \left\{ \left(\frac{\kappa}{\overline{c_p} \mu} \frac{\rho \mu}{\rho_e \mu_e} \right) \left[L_{e_i} Y_{i\eta} + L_{e_i}^T Y_i \frac{\theta_\eta}{\theta} \right] \right\}_\eta \\ &= \frac{\rho u_e^2 x^{2n}}{2\xi} c_{i,e} \rho_e \mu_e \left[\left(\frac{C}{P_r} \right) \left(L_{e_i} Y_{i\eta} + L_{e_i}^T Y_i \frac{\theta_\eta}{\theta} \right) \right]_\eta \end{aligned} \tag{A.26}$$

Dividing each term by $\rho_e \mu_e \rho u_e^2 x^{2n} c_{i,e} / 2\xi$, we get

$$\left(\frac{C}{P_r} L_{e_i} Y_{i\eta}\right)_\eta + f Y_\eta + \left(\frac{C}{P_r} \frac{L_{e_i}^T Y_i}{\theta} \frac{d\theta}{d\eta}\right)_\eta + \frac{1}{(n+1)a} \frac{\dot{w}_i'''}{\rho c_{i,e}} = 2\xi\left(f_\eta f_{\eta\xi} - f_\xi f_{\eta\eta}\right) \tag{A.27}$$

If we neglect derivatives with respect to ξ , we have Equation (31).

$$\left(\frac{C}{P_r} L_{e_i} Y_{i\eta}\right)_\eta + f Y_\eta + \left(\frac{C}{P_r} \frac{L_{e_i}^T Y_i}{\theta} \frac{d\theta}{d\eta}\right)_\eta + \frac{1}{(n+1)a} \frac{\dot{w}_i'''}{\rho c_{i,e}} = 0 \tag{31}$$

This complete all the derivations.

APPENDIX B

THE TRANSPORT EQUATIONS

A. VISCOSITY

The viscosity of species i is given by the expression [26]

$$\mu_i = \frac{5}{16}\frac{\sqrt{\pi W_i K_B T}}{\pi \sigma_i^2 \Omega^{(2,2)^*}} \qquad (B.1)$$

where σ_i is the Lennard-Jones collision diameter, and W_i is the mass of the molecule. The collision integral $\Omega^{(2,2)^*}$ depends on the reduced temperature given by

$$T_i^* = \frac{K_B T}{\varepsilon_i} \qquad (B.2)$$

ar d the reduced dipole moment given by

$$\delta_i^* = \frac{1}{2}\frac{\tau_i^2}{\varepsilon_i \sigma_i^3} \qquad (B.3)$$

where τ_i is the dipole moment, ε_i is the Lennard-Jones potential well depth, and K_B is the Boltzmann constant. The integral value will be given by the quadradic interpolation of the previous experimental work by Monchick and Mason [27].

B. THERMAL CONDUCTIVITY

The thermal conductivities then follow from the expression [28]

$$\kappa_i = \frac{\mu_i}{M_i}\left(F_{trans}\, c_{v,trans} + F_{rot}\, c_{v,rot} + F_{vib}\, c_{v,vib}\right) \qquad (B.4)$$

where

$$F_{trans} = \frac{5}{2}\left(1 - \frac{2}{\pi}\frac{c_{v,rot}}{c_{v,trans}}\frac{\Gamma}{\Upsilon}\right) \qquad (B.5)$$

$$F_{\text{rot}} = \frac{\rho D_{ii}}{\mu_i}\left(1 + \frac{2}{\pi}\frac{\Gamma}{\Upsilon}\right) \tag{B.6}$$

$$F_{\text{vib}} = \frac{\rho D_{ii}}{\mu_i} \tag{B.7}$$

and

$$\Gamma = \frac{5}{2} - \frac{\rho D_{ii}}{\mu_i} \tag{B.8}$$

$$\Upsilon = U_{\text{rot}} + \frac{2}{\pi}\left(\frac{5}{3}\frac{c_{\text{v,rot}}}{R_{\text{U}}} + \rho\frac{D_{ii}}{\mu_i}\right) \tag{B.9}$$

The constant volume specific heat c_v relationships due to different excitation energy are dependent on whether the molecule is linear or not. For linear molecule, we have

$$\frac{c_{\text{v,rot}}}{c_{\text{v,trans}}} = \frac{2}{3} \tag{B.10}$$

$$\frac{c_{\text{v,rot}}}{R} = 1 \tag{B.11}$$

$$c_{\text{v,vib}} = c_v - \frac{5}{2}R \tag{B.12}$$

where c_v is the full constant volume specific heat of the molecule. In the case of a nonlinear molecule, we have

$$\frac{c_{\text{v,rot}}}{c_{\text{v,trans}}} = 1 \tag{B.13}$$

$$\frac{c_{v,rot}}{R_U} = \frac{3}{2} \tag{B.14}$$

$$c_{v,vib} = c_v - 3R_U \tag{B.15}$$

For single atoms (like H,O atoms), there are no molecule energy contribution due to rotation and vibration. Hence

$$\kappa_i = \frac{\mu_i}{M_i}\left(F_{trans}\frac{3}{2}R_U\right) \tag{B.16}$$

where $F_{trans} = 5/2$. For self-diffusion coefficient, we evaluate the following expression [26]

$$D_{ii} = \frac{3}{16}\frac{\sqrt{2\pi K_B^3 T^3/W_i}}{p\,\pi\,\sigma_i^2\Omega^{(1,1)^*}} \tag{B.17}$$

The rotational relaxation collision number U_{rot} is dependent on temperature. If data is available at 298K, we have

$$U_{rot}(T) = U_{rot}(298)\frac{\Lambda(298)}{\Lambda(T)} \tag{B.18}$$

where

$$\Lambda(T) = 1 + \frac{\pi^{3/2}}{2}\left(\frac{\varepsilon/K_B}{T}\right)^{\frac{1}{2}} + \left(\frac{\pi^2}{4} + 2\right)\left(\frac{\varepsilon/K_B}{T}\right) + \pi^{3/2}\left(\frac{\varepsilon/K_B}{T}\right)^{\frac{3}{2}} \tag{B.19}$$

C. DIFFUSION COEFFICIENTS

The binary diffusion coefficients can be evaluated from the following expression [26]

$$D_{ki} = \frac{3}{16}\frac{\sqrt{2\pi K_B^3 T^3 / W_{ki}}}{p\,\pi\,\sigma_{ki}^2\,\Omega^{(1,1)^*}} \tag{B.20}$$

where W_{ki} is the reduced molecular mass for the (k, i) species pair

$$W_{ki} = \frac{2W_kW_i}{W_k + W_i} \tag{B.21}$$

and σ_{ki} is the averaged collision diameter. In computing the averaged quantities, we consider two cases, depending on whether the collision partners are polar or nonpolar. For the case that partners are either both polar or both nonpolar, we assume

$$\frac{\varepsilon_{ki}}{K_B} = \sqrt{\left(\frac{\varepsilon_k}{K_B}\right)\left(\frac{\varepsilon_i}{K_B}\right)} \tag{B.22}$$

$$\sigma_{ki} = \frac{1}{2}(\sigma_k + \sigma_i) \tag{B.23}$$

$$\tau_{ki}^2 = \tau_k\tau_i \tag{B.24}$$

For the case of a polar molecule interacting with a nonpolar molecule, we have

$$\frac{\varepsilon_{np}}{K_B} = \zeta^2\left(\frac{\varepsilon_n}{K_B}\right)\left(\frac{\varepsilon_p}{K_B}\right) \tag{B.25}$$

$$\sigma_{np} = \frac{1}{2}(\sigma_n + \sigma_p)\zeta^{-\frac{1}{6}} \tag{B.26}$$

$$\tau_{np}^2 = 0 \tag{B.27}$$

where

$$\zeta = 1 + \frac{1}{4}\alpha_n^* \tau_p^* \sqrt{\frac{\varepsilon_p}{\varepsilon_n}} \tag{B.28}$$

In the above expression α_n^* is the reduced polarizability for the nonpolar molecule, and τ_p^* is the reduced dipole moment for the polar molecule. The reduced values are given by

$$\alpha_n^* = \frac{\alpha_n}{\sigma_n^3} \tag{B.29}$$

$$\tau_p^* = \frac{\tau_p}{\sqrt{\varepsilon_p \sigma_p^3}} \tag{B.30}$$

The following reduced parameters are required for the collision integral $\Omega^{(1,1)^*}$ evaluation

$$T_{ki}^* = \frac{K_B T}{\varepsilon_{ki}} \tag{B.31}$$

$$\delta_{ki}^* = \frac{1}{2}\tau_{ki}^{*\,2} \tag{B.32}$$

Now we introduce a correction factor to the binary diffusion coefficients [29]. Equation (B.4) becomes

$$D_{ki} = D_{ki}(1 + X_{ki}) \tag{B.33}$$

where the correction factor is given by

$$X_{ki} = \left(\frac{(6C^*_{ki} - 5)^2}{10} \right) \left(\frac{P_k + P_i + P_{ki}}{Q_k + Q_i + Q_{ki}} \right) \tag{B.34}$$

with

$$P_k = \frac{2W_i^2}{(W_i + W_k)W_i} \sqrt{\frac{2W_i}{W_k + W_i}} \frac{\Omega^{(2,2)*}_{kk}}{\Omega^{(1,1)*}_{ki}} \left(\frac{\sigma_k}{\sigma_i} \right)^2 \tag{B.35}$$

$$P_{ki} = 15 \left(\frac{W_k - W_i}{W_k + W_i} \right)^2 + \frac{8W_kW_iA^*_{ki}}{W_k + W_i} \tag{B.36}$$

$$Q_k = \left[(\frac{5}{2} - \frac{6}{5} B^*_{ki})W_k^2 + 3W_i^2 + \frac{8}{5} W_kW_iA^*_{ki} \right] \times \left[\frac{2}{W_i(W_k + W_i)} \sqrt{\frac{2W_i}{W_k + W_i}} \frac{\Omega^{(2,2)*}_{kk}}{\Omega^{(1,1)*}_{ki}} \left(\frac{\sigma_k}{\sigma_{ki}} \right)^2 \right] \tag{B.37}$$

$$Q_{ki} = 15 \left(\frac{W_k - W_i}{W_k + W_i} \right)^2 \left(\frac{5}{2} - \frac{6}{5} B^*_{ki} \right) + \frac{4W_kW_iA^*_{ki}}{(W_k + W_i)^2} \left(11 - \frac{12}{5} B^*_{ki} \right) \frac{8}{5} \frac{(W_k + W_i)}{\sqrt{W_kW_i}} \frac{\Omega^{(2,2)*}_{kk}}{\Omega^{(1,1)*}_{ki}} \frac{\Omega^{(2,2)*}_{ii}}{\Omega^{(1,1)*}_{ki}} \left(\frac{\sigma_k}{\sigma_{ki}} \right)^2 \left(\frac{\sigma_i}{\sigma_{ki}} \right)^2 \tag{B.38}$$

$$A^*_{ik} = \frac{\Omega^{(2,2)*}_{ik}}{\Omega^{(1,1)*}_{ik}} \tag{B.39}$$

$$B^*_{ik} = \frac{5\Omega^{(1,2)*}_{ik} + 4\Omega^{(1,3)*}_{ik}}{\Omega^{(1,1)*}_{ik}} \tag{B.40}$$

$$C^*_{ik} = \frac{\Omega^{(1,2)*}_{ik}}{\Omega^{(1,1)*}_{ik}} \tag{B.41}$$

D. THERMAL DIFFUSION RATIOS

The thermal diffusion ratios can be defined by introducing the thermal diffusion velocity

$$V_{i_v} = \frac{D_i \Theta_i}{X_i} \frac{1}{T} \frac{\partial T}{\partial x_v} \tag{B.42}$$

where x_v is a spatial coordinate and X_i is the mole fractions. We only consider the thermal diffusion for the species i whose molecular weight is less than 5. The thermal diffusion ratio is given by [30]

$$\Theta_i = \sum_{\substack{k=1 \\ k \neq i}}^{ns} \phi_{ki} \tag{B.43}$$

where

$$\phi_{ki} = \frac{15}{2} \frac{(2A^*_{ki} + 5)(6C^*_{ki} - 5)}{A^*_{ki}(16A^*_{ki} - 12B^*_{ki} + 55)} \frac{M_k - M_i}{M_k + M_i} X_k X_i \tag{B.44}$$

These are the semi-experimental approximations used in the transport properties evaluation.